Evidence for As contamination and the partitioning of Pd into pentlandite and Co + platinum-group elements into pyrite in the Fazenda Mirabela Intrusion, Brazil.

Robert D. Knight[1*], Hazel M. Prichard[1], and Cesar F. Ferreira Filho[2]

[1]School of Earth & Ocean Sciences, Cardiff University, Main Building, Park Place, Cardiff, CF10 3AT, UK

[2]Instituto de Geociência, Universidade de Brasília, Campus Universitário, Brasília-DF, 70910-900, Brazil

*R.D.Knight@soton.ac.uk

*Current address: Ocean & Earth Science, University of Southampton, Southampton, SO14 3ZH, UK

Abstract

The Fazenda Mirabela intrusion in Brazil hosts two zones of mineralization, the Santa Rita Ni-Cu-sulfide ore zone occurring predominantly in an orthopyroxenite layer, and an underlying basal platinum-group element (PGE) anomaly hosted in S-poor dunite. We show that in the northern and southern (marginal) zones of the intrusion, $(Pt,Pd,Ni,Cu)(Fe,Bi,Te)_2$ minerals are accompanied by As-bearing platinum group minerals (PGM) sperrylite ($PtAs_2$), and irarsite ([RhIrPt]AsS). These As-bearing PGM are extremely rare in the central zone of the intrusion, suggesting that As has been introduced into the margins of the intrusion from the country rocks via crustal assimilation or syn-magmatic hydrothermal processes. Other PGM and precious metal minerals (PMM) including hessite (Ag_2Te), Pd-Ag tellurides, electrum, and native Au are observed in the Santa Rita ore zone and do not show any lateral variation. In the semimetal-poor, S-poor dunite hosting the basal PGE anomaly, PGE are predominantly retained in the base metal sulfides and only minor PGE alloys are present. In this S-poor dunite Pt, Au and semimetals partitioned into a fractionated Cu-rich liquid which formed during the crystallization of monosulfide solid solution (MSS) and was largely removed by high temperature magmatic fluids. Palladium was not affected by this process and significant concentrations of Pd are identified in pentlandite, suggesting that Pd preferentially partitioned into MSS as it crystallized and subsequently pentlandite as it exsolved. Pyrite in the Santa Rita ore zone is Co-rich and contains higher concentrations of IPGE (Os, Ir, Ru) and Rh than pyrrhotite and pentlandite, suggesting that pyrite has not replaced and inherited the PGE concentrations of these sulfides. The Pd-poor nature of pyrite also indicates that it has not replaced Pd-rich pentlandite. It is proposed that the IPGE and Co preferentially partitioned into pyrite as it exsolved from MSS.

Keywords: Fazenda Mirabela, Platinum-group elements, Sulfide, Pyrite, Arsenic

Introduction

The Fazenda Mirabela ultramafic-mafic layered intrusion located in Bahia State, north-eastern Brazil (Fig. 1), hosts the stratiform Santa Rita Ni-Cu-sulfide ore zone (Barnes et al., 2011; Inwood et al., 2011). This ore zone varies in thickness up to 200 m and is

situated within the upper part of the ultramafic sequence, close to the boundary with the mafic sequence, and hosts appreciable concentrations of platinum-group elements (PGE) with Pt + Pd typically between 0.1-0.5 ppm. A second zone of sulfur-poor PGE mineralization underlies the Santa Rita ore zone and is referred to herein as the 'basal PGE anomaly' following the nomenclature of Barnes et al. (2011).

The Santa Rita ore zone has extremely high Ni tenors while remaining relatively PGE-poor. The formation of this deposit and its Ni-rich nature has been attributed to the prolonged mixing of an initially magnesian, moderately Ni-enriched resident "M-type magma" close to sulfide saturation, with a relatively Ni-PGE-depleted and cooler replenishing "G-type magma" charged with suspended sulfide liquid droplets (Barnes et al., 2011). A contributing factor in forming high Ni tenors may be the reaction between the sulfide liquid and coexisting olivine in an environment where both phases equilibrate with a large reservoir of silicate magma; furthermore, higher Ni content in the sulfide liquid gives rise to an increased tendency for Ni to partition into sulfide from adjacent olivine, forming a positive feedback mechanism (Barnes et al., 2011).

The Fazenda Mirabela intrusion has been divided into three zones for mining purposes; central, southern, and northern (Fig. 2). The platinum-group mineralogy of 21 samples from two boreholes in the central zone of the intrusion has been documented by Knight et al. (2011). They identified Pt-Pd-Ni tellurides accompanied by Ag tellurides, minor electrum, and native Au in the both the Santa Rita ore zone and the underlying basal PGE anomaly, however, they also recognized a localized PGE alloy assemblage dominated by Pd-Cu alloys in samples from the basal PGE anomaly in one borehole. Here we build on this study by documenting the platinum-group minerals (PGM) and precious metal minerals (PMM) in samples from four new boreholes; two from the northern zone and two from the southern zone of the intrusion. Laser ablation (LA)-ICP-MS and whole-rock geochemical analyses have been completed on samples from the northern and southern zones as well as those from the central zone studied by Knight et al. (2011). These combined data fully characterize the PGE mineralization in the Fazenda Mirabela intrusion and are used to explain some unusual features of the Santa Rita ore zone and the underlying basal PGE anomaly.

Regional and Local Geology

Regional geology

The Fazenda Mirabela intrusion is part of a cluster of ultramafic-mafic complexes located in the southern portion of the Paleoproterozoic Itabuna-Salvador-Curaça belt. The latter comprises a low-K calc-alkaline plutonic suite formed during the collision of Archean blocks during the ~2.15-2.05 Ga Transamazonian orogeny (Barbosa and Sabaté, 2004). The immediate country rocks to the intrusion are comprised of a supracrustal sequence of gneisses and minor metamorphosed banded iron formations, metabasic sills, as well as a deformed sequence of granulite facies charnockite and enderbite orthogneisses (Fig. 1; Barbosa et al., 2003). The intrusion of the largely unaltered and undeformed Fazenda Mirabela and Palestina igneous bodies (~2065 Ma; Ferreira Filho et al., 2013) postdates the regional granulite facies metamorphism of the country rocks (2086 ± 7 Ma; Peucat et al., 2011).

Stratigraphy of the Fazenda Mirabela intrusion

The north-easterly dipping Fazenda Mirabela intrusion covers a surface area of ~7 km^2 and consists primarily of a lower ultramafic sequence exposed to the west and an upper mafic sequence exposed to the east (Fig. 2). Individual layers become progressively thinner towards the southern and northern borders (Ferreira Filho et al., 2013). The stratigraphic base of the Fazenda Mirabela intrusion is a reversely differentiated sequence comprising ~90 m of gabbronorite overlain by ~150 m of orthopyroxenite. These units are overlain by the ultramafic sequence (~750 m thick), consisting of ~600 m of dunite followed by a ~ 150 m sequence of harzburgite, olivine orthopyroxenite, and orthopyroxenite that is capped by a thin 1-2 m websterite unit. The thickness of individual layers in the upper portion of the ultramafic sequence is variable and characterized by interlayered rock types (Ferreira Filho et al., 2013). This is overlain by the mafic sequence (~1300 m thick) comprised of monotonous gabbronorite. The intrusion shows no evidence of the high-grade metamorphism and deformation that has affected the surrounding country rocks, but has been cross-cut by late minor dolerite and felsic pegmatitic dykes. Significant laterization has occurred at the surface of the intrusion, particularly over the lower (or western) ultramafic sequence (Inwood et al., 2011).

Mineralization

The Santa Rita Ni-Cu-(PGE) sulfide orebody is a semi-continuous stratabound zone of disseminated sulfides situated within the upper ~100 m of the ultramafic sequence, predominantly in the orthopyroxenite unit (excluding the uppermost part of this lithology), extending down into the upper part of the harzburgite (Barnes et al., 2011). The orebody varies in thickness and in its exact position within the igneous stratigraphy from the north to the south of the intrusion. The ore zone occurs as a single well-defined layer ~50 m thick in the northern part of the intrusion and transitions into a thick (up to ~200 m) discontinuous zone at the southern margin of the intrusion while transgressing upwards through the ultramafic stratigraphy (Barnes et al., 2011). The ore zone typically consists of 0.5-3.0 vol. % disseminated sulfides, and is PGE bearing with Pt + Pd concentrations typically between 0.1-0.5 ppm (Fig. 3). The base metal sulfide (BMS) assemblage is dominated by pentlandite (~50%) which is accompanied by variable but progressively lesser amounts of pyrite, pyrrhotite, and chalcopyrite. The combined proven and probable reserves of the Santa Rita deposit as of 31 December 2010 stood at 159 million metric tons at 0.52 wt. % Ni, 0.13 wt. % Cu, 0.015 wt. % Co, and 86 ppb Pt (Mirabela Nickel Ltd., Annual Report, 2011).

Primary magmatic minerals and textures are well preserved (Fig. 4). Two main types of sulfide morphology are observed: i) BMS occurring interstitially to olivine and orthopyroxene crystals (Fig. 4A-B), and ii) small fine grained sulfides which are intergrown with fine grained intercumulus silicate phases (plagioclase, clinopyroxene and phlogopite). Interstitial sulfides exhibit low dihedral angles, but more commonly have rounded terminations that were previously noted by Barnes et al. (2011) who also described the silicate mineralogy and chemistry in greater detail. Interstitial sulfide blebs (typically ~1 mm across) consist of cores of pentlandite, usually intergrown with euhedral pyrite (Fig. 4C),

partially surrounded by chalcopyrite and pyrrhotite. Minor BMS are also observed within the separated cleavage planes of orthopyroxene crystals.

Sulfide stringers composed of pentlandite, pyrrhotite, and chalcopyrite are observed extending from interstitial sulfides. These are often only a few microns wide and are commonly aligned, giving rise to a pseudo-fabric within the rock. Minor localized patches and veins of post-magmatic serpentinisation are observed in the Santa Rita ore zone and in some cases these are associated with the BMS stringers.

A zone of S-poor (<0.1 wt. % S) PGE mineralization forming the basal PGE anomaly is observed in the upper part of the dunite, underlying the Santa Rita ore zone (Fig. 3). This dunite displays a decoupling of S and PGE, with Pt and Pd tenors for this zone calculated to be significantly higher (~20 ppm for both Pt and Pd) than those of the relatively BMS-rich Santa Rita ore zone (Barnes et al., 2011). The basal PGE anomaly typically occurs between 50-75 m below the base of the Santa Rita ore zone and is observed in the central zone and southern zone boreholes; the depth of the northern zone boreholes is not sufficient to intersect this anomaly. The sulfides are finely disseminated forming small (< 150 µm across) interstitial crystals dominated by pentlandite accompanied by minor chalcopyrite, with pyrrhotite and pyrite virtually absent (Fig. 4D). Micro-scale sulfide-silicate graphic textures that resemble symplectites are commonly observed (Fig. 4E-F) and are often associated with phlogopite.

Sampling and Analytical Methods

Drill core from four boreholes was sampled; two from the northern zone (MBS209 and MBS158; samples PTSR26-49) and two from the southern zone (MBS565 and MBS569; samples PTSR50-72). Borehole locations and additional information are given in Figure 2 and Table 1, respectively. Sampling was completed with the aid of mine assay data to identify samples with the highest PGE contents and was extended ~100 m above and below the defined economic limits of the Santa Rita ore zone in order to sample all lithologies present in the intrusion, and the basal PGE anomaly where intersected.

A total of 47 samples were collected; 12 from each borehole sampled, except for MBS565 where only 11 samples were taken as a sample of gabbronorite could not be obtained from this hole. The silicate and sulfide mineralogy of all samples were characterized using transmitted and reflected light microscopy of polished thin sections. Detailed analysis of the platinum-group mineralogy was conducted on 40 samples; gabbronorite and websterite samples were not studied given their low PGE concentrations. Platinum-group and precious metal minerals and their associated sulfide, silicate, and oxide minerals were identified and analyzed using a Cambridge Instruments (now Carl Zeiss NTS) S360 scanning electron microscope (SEM). Polished thin sections were searched systematically for PGM using the SEM set at a magnification of 100x. Quantitative analyses of the larger PGM (> 0.3 x 0.3 µm) were obtained using an Oxford Instruments INCA Energy EDX analyzer attached to the SEM. Operating conditions for the quantitative analyses were 20 kV, with a specimen calibration current of ~1 nA and a working distance of 25 mm. A cobalt reference standard was regularly analyzed in order to check for any drift in the analytical conditions. A comprehensive set of standards obtained from MicroAnalysis Consultants Ltd. (St Ives,

Cambridgeshire) were used to calibrate the EDX analyzer. Semi-quantitative analyses of smaller PGM (< 0.3 x 0.3 µm) were determined by accounting for elements derived from the host minerals. Images were obtained using a four-quadrant back-scattered detector operating at 20 kV, a beam current of ~500 pA, and a working distance of 13 mm, under which conditions, magnifications of up to 15000x are possible.

Commercial mine assay data were obtained from one meter composite intervals of diamond drill core by ALS Chemex Ltd., Vancouver, Canada. Fire assay was used to determine Au, Pt, and Pd by ICP-MS finish while multi-element ICP-MS was used to obtain data for the other elements reported here.

Whole-rock PGE (excluding Os) and Au data were determined by Actlabs via Ni-fire assay for all samples from the northern and southern zones (PTSR26-72) as well as samples from the central zone (PTSR01-25 from boreholes MBS604 and MBS605; Fig. 2) studied by Knight et al. (2011). Semimetal concentrations (As, Bi, Sb, Te) were determined by aqua regia digest and ICP-MS finish by Actlabs for samples PTSR26-72 from the northern and southern zones of the intrusion.

A selection of 31 samples from all six boreholes studied (central, northern and southern zones) from both the Santa Rita ore zone and the underlying basal PGE anomaly were analyzed using LA-ICP-MS at Cardiff University. This was carried out using a New Wave Research UP213 UV laser system coupled to a Thermo X Series 2 ICP-MS. Platinum-group elements and other elements were determined in time-resolved analysis mode (time slices of 350 ms) as the laser beam followed a line designed to sample different sulfide phases. The beam diameter employed was 30 µm, with a frequency of 10 Hz, and the sample was translated at 6 µm/s relative to the laser. Acquisitions lasted between 80-400 s, and a gas blank was measured for 30-40 s prior to analysis. The internal standard used was ^{33}S and this was measured for the analyzed sulfides quantitatively using the SEM. Subtraction of gas blanks and internal standard corrections were performed using Thermo PlasmaLab software.

In order to show that these analyses represent PGE in solid solution, laser traces that indicated higher than average Te or As concentrations coupled with anomalously high PGE have been discounted from the data set as it is likely that PGM (predominantly Te- or As-bearing PGM) were intercepted in these cases. Similarly, analyses have also been discounted where the time resolved spectra have clearly indicated the presence of PGM or PGM micro-inclusions.

Calibration was performed using five synthetic Ni-Fe-S standards prepared from quenched sulfides. The standards incorporate S, Ni, Fe, and Cu as major elements and Co, Zn, As, Se, Ru, Rh, Pd, Ag, Cd, Sb, Te, Re, Os, Ir, Pt, Au, and Bi as trace elements. The compositions of these sulfide standards are given in Prichard et al. (2013). The standards produce five point calibration curves for S, Ni, and Fe. Standards 1, 4, and 5 produce three point calibration curves for the PGE, Ag, Cd, Re, Au, and semimetals. Standards 1-3 produce three point calibration curves for Cu, Co, and Zn, and reliable matrix-matched corrections for argide species ($^{59}Co^{40}Ar$, $^{61}Ni^{40}Ar$, $^{63}Cu^{40}Ar$, $^{65}Cu^{40}Ar$, $^{66}Zn^{40}Ar$) that interfere with light PGE isotopes. Corrections for ^{106}Cd on ^{106}Pd and ^{108}Cd on ^{108}Pd were determined using Standard 1. Where independent corrections have been applied to different isotopes of the same element (e.g., $^{66}Zn^{40}Ar$ on ^{106}Pd and ^{108}Cd on ^{108}Pd) the independently corrected values vary by <20% (and commonly <5%) indicating that these corrections are robust. The

accuracy of the LA-ICP-MS procedure for PGE was checked by the analysis of the Laflamme-Po724 standard run as an unknown against the Cardiff sulfide standards at the start and end of each day.

Results

Whole-rock PGE and semimetal concentrations

Three distinct patterns are shown in the Fazenda Mirabela whole-rock PGE data plotted as chondrite normalized profiles, using the values given in Lodders (2003). They all have positive trends but exhibit variations in Pd, Pt, and Au concentrations. Pattern A is defined by negative Pd anomalies and is typically observed in orthopyroxenite, olivine orthopyroxenite, and harzburgite samples from the Santa Rita ore zone. Pattern B is defined by positive slopes without any significant anomalies and occurs primarily in harzburgite samples in the transition zone between the Santa Rita ore zone and the underlying basal PGE anomaly. Pattern C is defined by positive Pd and negative Au (and Pt) anomalies and typically occurs in samples from the basal PGE anomaly in the S-poor dunite. It is not feasible to show all whole-rock PGE patterns for every sample analyzed, so an example is given using the samples from borehole MBS569 in the southern zone in conjunction with a stratigraphic section showing the locations of the samples and where these different PGE patterns occur in the Fazenda Mirabela stratigraphy (Fig. 5).

Data from the central and southern zone boreholes is shown graphically using two plots of Pt/Pd versus Pd/Ru and Au/Pd versus Pd/Ru (Fig. 6); northern zone boreholes have been omitted as the stratigraphy is slightly more complex. These plots demonstrate that S-poor dunite samples from the basal PGE anomaly have low Pt/Pd and Au/Pd ratios, whereas samples above this zone, including the Santa Rita ore zone, have high Pt/Pd and Au/Pd ratios.

Whole-rock semimetal concentrations (As, Bi, Sb, and Te) for all samples studied from southern boreholes MBS565 and MBS569 (Table 2) reveal that Bi and Sb concentrations are very low and considered insignificant in the majority of samples studied. However, meaningful As and Te concentrations are noted and these correlate closely with S (Fig. 7). An understanding of the distribution of the whole rock concentrations of these semimetals throughout the intrusion is important as they control the PGE mineralogy.

Platinum-group and precious metal mineralogy

More than 500 platinum-group and precious metal minerals have been documented in the northern and southern zones of the Fazenda Mirabela intrusion (Table 3) and quantitative analyses of these PGM have been undertaken where possible (Table 4). A further 217 PGM and PMM were identified in the central zone of the intrusion (Knight et al., 2011). Three distinct PGM assemblages are observed in the Fazenda Mirabela intrusion which are described below. The location of all three PGM assemblages is provided in Figure 8.

Marginal assemblage

The marginal PGM assemblage is observed in the northern and southern zones of the intrusion and consists of $(Pt,Pd,Ni,Cu)(Fe,Bi,Te)_2$ minerals and As-bearing PGM, predominately sperrylite ($PtAs_2$) and members of the hollingworthite-irarsite-platarsite solid solution series ([RhIrPt]AsS). Minor Ag-Pd-Te minerals, electrum ± Fe-Cu, and native Au grains are observed, with accessory hessite (Ag_2Te) common.

Throughout the Santa Rita ore zone, the BMS occur interstitially to the silicates (Fig. 4A-B) with stringers composed of pentlandite, pyrrhotite, and chalcopyrite that extend from the interstitial BMS into the silicates along grain boundaries and occasionally along separated cleavage planes in orthopyroxene. Platinum-group minerals occur within BMS, on their margins, and in BMS stringers. The BMS stringers host both PGE-bearing tellurides (Fig. 9E-F) and sperrylite (Fig. 10D-E). These stringers connect to interstitial composite sulfides and PGM are observed both proximally (Fig. 9F and 10D) and distally (Fig. 9E and 10E) to the interstitial sulfides. The stringers are roughly aligned producing a pseudo-fabric in the rock and may be enclosed by serpentine in some occurrences (Fig. 9E).

Despite the presence of arsenides, the most common PGM (n=322) identified in the marginal assemblage belong to the $(Pt,Pd,Ni)(Fe,Bi,Te)_2$ solid solution series (Table 3) and vary in size from 0.5-639.6 μm^2 (avg. 30.1 μm^2). In the absence of Fe and Bi, these PGM are merenskyite ($PdTe_2$), moncheite, ($PtTe_2$), and melonite ($NiTe_2$). The proportions of Pt:Pd:Ni in these PGM have been plotted on a ternary diagram using semi-quantitative atomic weight data collected using the SEM (Fig. 11). This plot shows the abundance of Ni-dominant PGM which is in keeping with the high Ni content of the system as demonstrated by the proportion of pentlandite to other sulfide phases. These PGE-bearing tellurides are typically rounded (Fig. 9A-B) or lath shaped (Fig. 9C-D) with the majority associated with BMS (Fig. 13). These PGM are observed enclosed by a single sulfide phase (Fig. 9A-B), crossing sulfide phase boundaries (Fig. 9C), and as laths at the edge of BMS and in contact with adjacent silicates (Fig. 9D). In contrast to the central zone, Cu-bearing tellurides are observed (CuTe) and Cu also substitutes for Pt, Pd, and Ni in some PGM (Table 4).

The major difference in the platinum-group mineralogy between the margins of the intrusion and the central zone is the significant increase in As-bearing PGM observed at the margins. Sperrylite crystals are relatively abundant, with 69 identified in the northern and southern zones compared to four in the central zone. They typically range in size between 0.8-463.3 μm^2 with smaller crystals occurring more regularly. The largest sperrylite identified falls outside of this range and is ~1.5 mm^2. Sperrylite is commonly situated within, or closely associated with the BMS (Fig. 10A-D) with only 20% of identified grains observed wholly within silicate or oxide phases. These PGM are euhedral with tabular forms when not hindered by the host sulfide.

Platinum-group minerals that belong to the hollingworthite-irarsite-platarsite solid solution series ([RhIrPt]AsS) have also been identified (Fig. 10F); 18 in the northern and southern zones compared to three in the central zone. Ten are Ir-dominant, all of which are Pt-bearing. Five are Pt-dominant, four of which are Ir-bearing, and one is Rh-bearing. The remaining three are Rh-dominant and are slightly more complex with the addition of Os (Rh-Ir-Pt-As-S, Rh-Pt-Os-As-S, Rh-Pt-Os-Ir-As-S). The size range of these PGM is relatively small, between 0.6-7.7 μm^2, with only one crystal larger than this range identified at 14.4 μm^2. The majority of these PGM (85%) are located at the edge of, or within BMS (Fig. 10F),

with only four identified in silicates; two of which retain a close association with sulfides (Fig. 13).

Two types of silver tellurides are observed, hessite which is common, and rarer Ag-Pd-Te. Hessite crystals range in size from 0.3-248.9 μm^2 (avg. 16.2 μm^2). These tellurides are typically subhedral-anhedral with a minority exhibiting lath crystal forms. They are predominantly observed within BMS (Fig. 12A-B) and rarely in silicates. The Ag-Pd-Te crystals exhibit the same behavior and crystal forms as hessite, however, they are less common and smaller, between 0.7-17.5 μm^2 (avg. 5.3 μm^2).

Several different types of Au-bearing alloys have been identified which are commonly associated with BMS and consist of electrum, Au-Cu, Au-Ag-(Cu-Fe) (Fig. 12C), and native Au (Fig. 12D). These Au-bearing alloys are typically anhedral and the majority range in size between 0.4-126.7 μm^2 (avg. 13.6 μm^2).

Five Pt-S minerals have been identified which are extremely variable in size between ~4-110 μm^2. They exhibit subhedral-euhedral crystal forms including three which are lath shaped. Three are situated within BMS while the remaining two are found in a silicate and oxide phase, respectively. Rare PGE-bearing alloys have also been identified which include one of each of the following; Pd-Cu, Ru-Os, Pt-Fe, and Pt-Ir. These PGE alloys are relatively small (<6 μm^2) and are all located within BMS.

Central zone assemblage

The central zone assemblage contains predominantly $(Pt,Pd,Ni)(Fe,Bi,Te)_2$ accompanied by accessory hessite (Ag_2Te), rare electrum and native Au grains observed in both the Santa Rita ore zone and the basal PGE anomaly in the underlying S-poor dunite in one borehole only (MBS605) (Knight et al., 2011). Platinum-group and precious metal mineral sizes, textures, and mineral associations are identical to the same minerals described in the marginal zones above. The main difference in PGM between the central zone and the northern and southern zones of the intrusion is the almost complete absence of As-bearing PGM in the central zone.

Localized PGE alloy assemblage

In the basal PGE anomaly hosted in the S-poor dunite and underlying the Santa Rita ore zone, a localized PGE alloy assemblage is observed only in one borehole (MBS604) in the central zone. This assemblage comprises predominately Pd-Cu-(Pb) alloys (Fig. 12E-F) accompanied by minor PGE-bearing arsenides (Knight et al., 2011). The PGM are associated with pentlandite and chalcopyrite, effectively the only two sulfide phases present in the S-poor dunite zone. PGM exhibit subhedral-euhedral forms where they are associated with unaltered fresh magmatic sulfides as in the Santa Rita ore zone. However, PGM are also associated with BMS exhibiting micro-scale sulfide-silicate graphic textures resembling symplectites, and in these cases the PGM are typically situated at the crystal edges and exhibit anhedral crystal forms (Fig. 12E-F).

PGM abundance and size distribution

The difference in mineralogy between the central zone (excluding the Pd-Cu alloy assemblage) and the margins of the intrusion are illustrated by pie charts based on both the number of each PGM and PMM type identified, and the combined surface area each PGM and PMM type identified (Fig. 14A-D); the Pd-Cu alloy assemblage is plotted separately (Fig. 14E-F). These plots demonstrate the significant variation in As-bearing PGM across the intrusion and the dominance of PGE alloys in the localized Pd-Cu alloy assemblage.

The abundance and size of PGM and PMM identified in the Fazenda Mirabela intrusion, including data from the central zone of the intrusion, varies between the Santa Rita ore zone and the underlying basal PGE anomaly in the S-poor dunite, regardless of which PGM assemblage is present. In the Santa Rita ore zone, PGM and PMM are larger, typically ranging between 1-24.9 μm^2 and are more abundant with ~17 PGM and PMM identified per sample (thin section) studied (Fig. 15). In the underlying S-poor dunite, the PGM and PMM are smaller, with >80% of those identified < 8.9 μm^2. They are also much less abundant with only ~5 PGM and PMM identified per sample (thin section) studied (Fig. 15).

Laser ablation-ICP-MS

Laser ablation analyses of the sulfides show the presence of PGE-poor BMS in the Santa Rita ore zone, and PGE-rich BMS in the basal PGE anomaly in the S-poor dunite (Table 5; Fig. 16).

Santa Rita ore zone

In the Santa Rita ore zone, the BMS host very low concentrations of PGE in solid solution. In both chalcopyrite and pyrrhotite, the average concentrations of all six PGE individually are <1 ppm. The highest Rh and Pt concentrations recorded in any sulfide phase are 1.1 ppm (pentlandite) and 1.6 ppm (pyrrhotite), respectively. Osmium concentrations can be relatively high (up to 4.5 ppm), however, these values are rare as evidenced by a low average value of <1 ppm. Pentlandite is the principal host of the PGE, with Pd concentrations of up to 13 ppm and an average value of 2.3 ppm; pentlandite also hosts low but significant average concentrations of Os (0.52 ppm) and Ru (0.91 ppm). More unusual is the identification of Os, Ir, Ru, and Rh in pyrite (Fig. 16A), with concentrations of up to 2.2 ppm Os, 1.0 ppm Ir, 3.7 ppm Ru, and 0.8 ppm Rh recorded, and average values of 0.6 ppm, 0.2 ppm, 0.8 ppm, and 0.1, respectively. Furthermore, pyrite also consistently hosts significant concentrations of cobalt, between 0.8-3.2 wt. %. Time resolved spectra show that concentrations of these PGE and Co in pyrite are not the result of intersecting discrete PGM or other mineral phases (Fig. 17A).

Basal PGE anomaly

The BMS analyzed from the S-poor dunite host very high concentrations of PGE. Pentlandite is the most PGE-enriched sulfide in these samples hosting high average concentrations of all six PGE (Fig. 16B); 4.2 ppm Os, 1.7 ppm Ir, 6.3 ppm Ru, 4.3 ppm Rh,

4.3 ppm Pt, and 42.5 ppm Pd. The highest concentrations identified are as follows; 38.3 ppm Os, 28.7 ppm Ir, 59.1 ppm Ru, 36.1 ppm Rh, 254 ppm Pd, and 28.9 ppm Pt. Time resolved spectra show that high concentrations of Pd, Ir, and particularly Pt in pentlandite are not the result of intersecting discrete PGM or other mineral phases (Fig. 17B).

In the basal PGE anomaly, chalcopyrite is the least PGE enriched sulfide and contains low average concentrations (<1 ppm) of Os, Ir, Ru, Rh, and Pt, but significant average concentrations of Pd (8.8 ppm). One of two pyrite crystals analyzed contains significant concentrations of IPGE (6 ppm Os, 2.5 ppm Ir, and 5.6 ppm Ru) while being poor in Rh, Pt, and Pd, however, the second pyrite crystal analyzed is generally PGE-poor with individual PGE concentrations all <1 ppm. These results are not statistically significant as only three chalcopyrite crystals and two pyrite crystals were analyzed due to the small size and rarity of these phases, respectively.

In many cases, quantitative analyses of individual sulfide phases could not be completed in this zone due to the small size of the sulfides and the resulting overlap of signals from adjacent silicates and oxides. Where interstitial sulfides were ablated, the signals of more than one sulfide phase often overlapped and could not be distinguished from one another to allow for the quantification of PGE in each individual phase. Therefore, average PGE concentrations were determined from the combination of two or three sulfide phases where signals from silicate and oxides minerals were absent. In these cases, the analyses are reported as BMS mixtures, most commonly a mixture of pentlandite and chalcopyrite (e.g., Pn-Cpy; Table 5). These composite sulfide analyses have been ignored in the Santa Rita ore zone for clarity, where all sulfide phases are large and relatively common, but have been included for the S-poor dunite samples given their significant PGE content and the rarity of relatively large mono-phase sulfides in this zone.

Average concentrations of PGE in pentlandite-chalcopyrite BMS mixtures are relatively high at 1.2 ppm Os, 3.3 ppm Ru, 2.2 ppm Rh, 2.6 ppm Pt and 42.4 ppm Pd, with ranges given in Table 5. However, these sulfides are Ir-poor with an average concentration of only 0.6 ppm. The highest Pd concentrations identified overall are 371 ppm and 570 ppm occurring in two other BMS mixtures consisting of pentlandite-pyrite and pentlandite-pyrite-chalcopyrite, respectively.

Discussion

This investigation into the PGE mineralization in the Fazenda Mirabela intrusion has revealed several interesting results that require discussion. These include: the variation from predominately PGE tellurides in the central zone to a combination of PGE-bearing tellurides and arsenides in the northern and southern zones (margins) of the intrusion, as well the overall genesis of these PGM; the formation of BMS stringers and their associated PGM; the formation of high PGE tenor sulfides in a system with relatively low PGE concentrations; and the origin of significant IPGE, Rh, and high Co concentrations in pyrite.

Formation of Te- and As-bearing PGM

The PGE-bearing tellurides are typically rounded and lath shaped, and probably formed via the exsolution of Pt, Pd, Ni, and Te from BMS (Knight et al., 2011) as suggested for these minerals both experimentally (Peregoedova et al., 2004) and naturally during the slow cooling intrusions (Barnes et al., 2008). Alternatively, Knight et al. (2011) suggested that these PGM crystallized directly from a late stage fractionated semimetal-rich liquid into which Pt, Pd, and excess Ni were concentrated during the crystallization of monosulfide solid solution (MSS) and intermediate solid solution (ISS). This suggestion is based on the incompatibility of these PGE with MSS (e.g., Fleet et al., 1993; Li et al., 1996; Ballhaus et al., 2001; Mungall et al., 2005) and ISS (Peregoedova, 1998), particularly in the presence of semimetals, specifically Te (Helmy et al., 2007; Holwell and McDonald, 2007; Hutchinson and McDonald, 2008; Helmy et al., 2010).

The timing of formation of the As-bearing PGM (sperrylite and members of the hollingworthite-irarsite-platarsite solid solution series) in the Santa Rita marginal ore zone deserves consideration (Fig. 8 and 10). These types of As-bearing PGM when observed completely enclosed by silicates and oxides are often interpreted to have crystallized early, directly from an immiscible sulfide melt and are then trapped in these later crystallizing phases (e.g., Coghill and Wilson, 1993; Hutchinson and McDonald, 2008; McDonald, 2008; Dare et al., 2010a). However, these PGM may maintain an association with BMS if, for instance, they do not cleanly separate from the sulfide liquid from which they have crystallized. This may have occurred in the Fazenda Mirabela intrusion where the majority of these PGM remain associated with BMS (Fig. 10A-D) and could explain why some sperrylite crystals are much larger than their host sulfides. In these cases, exsolution of PGE from the small BMS host could not account for PGM formation (Fig. 10C). It should be noted, however, that the observation of PGM larger than their host sulfide is two-dimensional and potentially not reliable. Sperrylite, where observed in primary magmatic BMS stringers, may have formed via exsolution from the sulfides during cooling; it is unlikely that they crystallized early in stringer form before the crystallization of the silicates (Fig. 10D-E).

The spatial variation in sperrylite and irarsite across the intrusion whereby these As-bearing PGM are restricted to the northern and southern margins may be explained by the possible addition of As from the surrounding country rocks via crustal assimilation. Crustal assimilation is a widely accepted process by which sulfide saturation can be achieved in ultramafic-mafic systems evidenced by: non-mantle sulfur isotopes ratios (e.g., Noril'sk and Duluth; Ripley, 1981; Ripley and Aljassar, 1987; Li et al., 2003); the association of magmatic sulfides with xenoliths (e.g., Voisey's Bay and Duluth; Ripley and Alawi, 1986; Mariga et al., 2006); and the association of sulfide ores with evaporites (e.g., Noril'sk ; Naldrett et al., 1992). Recently, this process has been examined in detail at Duluth by Samalens et al. (2017), who found that the contamination of the mafic magma by both sulfur and the semimetals results from the transfer of sulfide droplets from country rock xenoliths in a mobile, silicate partial melt.

Increased As concentrations have been linked to the local assimilation of country rocks (Ames and Farrow, 2007), and crustal assimilation is thought to be responsible for the localized crystallization of As-bearing PGM in both the Creighton deposit, Sudbury (Dare et al., 2010a), and the Platreef in the Bushveld Complex (Hutchinson and McDonald, 2008). The distribution of As-bearing PGM in the Fazenda Mirabela intrusion is also localized and restricted to the intrusion margins where the assimilation of country rocks may have occurred

during a period of limited magma mixing. The immediate country rocks to the Fazenda Mirabela intrusion include metamorphosed black shales (now present as graphite- and pyrite-bearing gneisses) which are often considered to be sources of As, S, and other semimetals (e.g., Hutchinson and McDonald, 2008). Although there is no direct evidence for the assimilation of As-bearing crustal rocks at Fazenda Mirabela, such as the presence of sulfarsenides or As-bearing PGM concentrated around crustal xenoliths, it is difficult to understand how the distinct zoning of As in the intrusion could have been achieved otherwise. It is possible that the syn-hydrothermal processes associated with the heat of magma emplacement resulted in the devolatilization of the country rocks and subsequent release of As (Hutchinson and McDonald, 2008) which was then introduced into the intrusion margins. This process would not require large amounts of assimilation via melting of the country rocks.

BMS stringers and associated PGM

Sulfide stringers with associated PGM extending from interstitial BMS characterize the mineralization in the Santa Rita ore zone. It appears that both the BMS and PGE have been distributed together into these stringers which originate from the interstitial BMS, as suggested by their close association.

One possible explanation for the formation of these sulfide stringers and their associated PGM is that they are the result of post-magmatic hydrothermal remobilization. At low temperatures (<500ºC), PGE ions will most likely complex with bisulfide (HS^-), however, bisulfide complexes are incapable of redistributing significant amounts of PGE unless fluid/rock ratios are very high with very effective depositional mechanisms (Hanley, 2005). In contrast, at high temperatures (>500^{o}C), chloride complexes are more likely to form (Hanley 2005). However, experiments by Wood and Normand (2008) demonstrate that unrealistically large amounts of oxidizing and acidic fluids are required to overcome the acid- and redox-buffering capacity of mafic, and by proxy ultramafic lithologies in order to mobilize palladium as a chloride complex.

It has been demonstrated that hydrothermal fluids may liberate PGE from their BMS hosts resulting in the formation of PGM. However, it is rare that the PGE are extensively remobilized and they are usually only transported very short distances (micrometers) in most cases (e.g., Prichard et al. 1994; Wang et al. 2008; Dare et al. 2010a; Prichard et al. 2013). Sulfur is typically much more mobile than the PGE, and in many examples where BMS and PGE have been affected by hydrothermal alteration, the BMS are remobilized or altered, resulting in either the exsolution of PGE in situ to form PGM associated with BMS or secondary phases (e.g., Prichard et al. 1994; Godel and Barnes, 2008a; 2008b; Prichard et al. 2013), or the isolation of preexisting PGM in secondary phases (e.g., Sá et al., 2005). However, the opposite has also been demonstrated in the Platreef, where late stage fluids have remobilized the PGE into the footwall in tremolite, talc, and serpentine as low temperature PGM assemblages that are devoid of sulfur (Armitage et al., 2002; Hutchinson and Kinnaird, 2005). The Waterberg deposit, South Africa, which shows many features typical of a low pressure epithermal system (Armitage et al., 2007) is perhaps the only example where large scale PGE (platinum) remobilization has occurred and is an atypical case (McDonald et al., 1999).

There is some evidence to suggest that these BMS stringers and their associated PGM are the product of hydrothermal remobilization. Many of the BMS stringers are associated with serpentine (Fig. 9E) indicating that post-magmatic hydrothermal alteration is responsible for their formation. However, if the sulfides had been affected or remobilized by hydrothermal processes, their composition should include secondary sulfides or magnetite (e.g., Godel and Barnes, 2008a; 2008b; Prichard et al., 2013; Smith et al., 2014). This is not observed as the stringers are composed of pentlandite, pyrrhotite, and chalcopyrite. Many studies have demonstrated that Pd is far more mobile than Pt (e.g., Fuchs and Rose, 1974; Prichard et al., 1994; 2001; Seabrook et al., 2004; Barnes et al., 2008; Wang et al., 2008; Suárez et al., 2010), thus one might expect Pd-bearing PGM to be dominant in these sulfide stringers. However, the PGM in the stringers are similar to those in the interstitial BMS including both Pt-bearing tellurides (Fig. 9E-F) and sperrylite (Fig. 10D-E). Therefore there is no evidence for the preferential remobilization of Pd over Pt. Furthermore, semimetal-bearing PGM are very insoluble compounds (Wood, 2002). It is therefore very unlikely that preexisting PGM associated with the interstitial sulfides have been remobilized into the sulfide stringers in the Fazenda Mirabela intrusion.

An alternative mode of formation for these BMS stringers and their associated PGM is that they represent the migration and crystallization of late-stage, PGE-bearing, fractionated sulfide liquids. This has been proposed for the formation of PGM-bearing veinlets observed in the Stillwater Complex (Zientek, 2002) and emanating from an immiscible sulfide bleb in a dyke in Uruguay (Prichard et al., 2004b). However, the composition of these stringers should be dominated by the recrystallization products of ISS such as chalcopyrite and other Cu-rich sulfides given the known fractionation of sulfide liquids (e.g., Hawley, 1965; Keays and Crocket, 1970; Naldrett et al., 1982; Holwell and McDonald, 2010), but pentlandite and pyrrhotite stringers are commonly observed (Fig. 9E).

A mechanical process whereby the sulfide liquid was compressed by the gravity settling and compaction of crystallizing silicates in the magma chamber best accounts for all observed features of the BMS stringers and their associated PGM. This compression forced a portion of the sulfide liquid, which at this point was coalescing as interstitial blebs (Fig. 18A-B), outwards through the crystal pile in the direction of least resistance along the boundaries of olivine and pyroxene crystals, either replacing any interstitial silicate melt or migrating through solidified silicates along their grain boundaries (Mungall and Su, 2005) giving rise to the observed alignment of the sulfide stringers. In some cases, it appears that the sulfide liquid has fractured crystallized silicates during its migration offsetting preexisting cracks (Fig. 9F). The unfractionated sulfide liquid then cooled and crystallized to form MSS and ISS in situ at sites interstitial to silicates and in stringers (Fig. 18C). This accounts for the primary composition of the stringers and the consistent chemistry of both the sulfides and their associated PGM across both the interstitial sulfides and BMS stringers (Fig. 18D).

Variation in PGM abundance and the origin of high tenor BMS

In the Santa Rita ore zone, semimetals are readily available (Fig. 7) resulting in the formation of abundant PGM, ~17 PGM per sample (thin section) studied, leaving the BMS PGE-poor (Table 5) as these elements exsolved from the sulfides during cooling to form PGM. The basal PGE anomaly in the S-poor dunite is semimetal-poor (Fig. 7), therefore

PGM do not readily form, with only ~5 PGM observed per sample (thin section) and the balance of PGE is retained in solid solution in high tenor sulfides (Table 5).

In the S- and semimetal-poor dunite, micro-scale sulfide-silicate graphic textures, very high PGE tenors, and an unusual BMS assemblage (pentlandite with minor chalcopyrite) cannot be explained by normal magmatic processes, particularly when compared to the Santa Rita ore zone. In an updated interpretation from that of Knight et al. (2011), we propose that small volumes of a magmatically derived, high temperature, volatile-rich (evidenced by the presence of phlogopite associated with sulfides exhibiting micro-scale sulfide-silicate graphic textures) fluid with a high oxygen fugacity (f_{O_2}) interacted with the sulfides in the dunite after the crystallization of MSS, but before the crystallization of ISS. This interaction resulted in the removal of significant amounts of Cu-rich fractionated sulfide liquid into which Pt, Au, and the semimetals preferentially partitioned during the crystallization of MSS (Fig. 19A), whereas the IPGE, Rh, and Pd partitioned into MSS as it crystallized (e.g., Fleet et al., 1993; Li et al., 1996; Ballhaus et al., 2001; Mungall et al., 2005; Barnes et al., 2006; Godel et al., 2007; Helmy et al., 2007; Holwell and McDonald, 2007; Helmy et al., 2010; Osbahr et al., 2013; Cafagna and Jugo, 2016). These high temperature fluids appear to have redistributed the Cu-rich liquid (including the Pt, Au, and semimetals therein; Fig. 19B), upwards into the Santa Rita ore zone, evidenced by the abundance of Te-bearing PGM and the consistent increase in Pt and Au concentrations relative to the other PGE (Fig. 5 and 6). The continued interaction of this magmatic fluid with crystallized MSS appears to have removed sulfide via melting or dissolution of Fe-sulfide by oxidizing the Fe to Fe_3O_4 while removing S as SO_2 or H_2S, resulting in the formation of magnetite (Fig. 19B) and other secondary minerals (Kinloch, 1982; Andersen, 2006) while creating the micro-scale sulfide-silicate graphic textures observed. The removal of Fe-sulfide resulted in Ni concentrations increasing in the remaining MSS, explaining the presence of pentlandite at the expense of pyrrhotite. The formation of PGM from MSS was extremely limited due to the removal of semimetals. Instead PGE remained in solid solution giving rise to high IPGE, Rh and Pd tenors in MSS, and subsequently pentlandite as it exsolved. During cooling, any remaining Cu-rich fractionated sulfide liquid crystallized to form ISS. Minor Au-Ag-Cu alloys and Te-bearing PGM exsolved on further cooling, while Pt diffused from ISS/chalcopyrite into pentlandite (Fig. 19C; Dare et al., 2010b; Piña et al., 2011).

These high temperature magmatic fluids appear to have interacted pervasively throughout the dunite, affecting all sulfides in this zone to some extent. However, there is evidence that this fluid was concentrated or channelized in some parts of the intrusion evidenced by the Pd-Cu alloy assemblage observed in borehole MBS604. In this localized basal zone of the intrusion, almost all of the fractionated Cu-rich sulfide liquid, including the Pt, Au, and semimetals therein, was removed (Fig. 19D) resulting in the formation of PGE-bearing alloys (predominantly Pd-Cu phases) in the absence of semimetals (Fig. 19E-F). The formation of alloys by desulfurization in other PGE-bearing systems has been reported, and is usually interpreted as a result of PGE being forced to exsolve during sulfur loss (Kinloch, 1982, Andersen, 2006; Li and Ripley, 2006; Godel and Barnes, 2008a). One would expect that sulfides hosting Pd-Cu alloys in the Fazenda Mirabela intrusion would therefore be depleted in Pd (e.g., Godel and Barnes, 2008a), however, it is impossible to test this by LA-ICP-MS without also ablating these alloys.

The presence of Pd in pentlandite

Many natural and experimental studies suggest that Pd partitions with Pt and Au into fractionated sulfide melts during the crystallization of MSS and ISS (e.g., Fleet et al., 1993; Li et al., 1996; Peregoedova, 1998; Ballhaus et al., 2001; Mungall et al., 2005), however, significant concentrations of Pd are commonly identified in pentlandite. Some researchers have suggested that Pd may partition into a Cu-rich liquid, either ISS or a late stage immiscible sulfide melt (Barnes et al., 2006) and that it subsequently diffuses into pentlandite from chalcopyrite during cooling via subsolidus exchange (Dare et al., 2010b; Piña et al., 2011). However, this does not explain high Pd concentrations in pentlandite crystals that are isolated from other BMS where this diffusion process cannot occur (e.g., Osbahr et al., 2013) and recent experimental work demonstrates that in the absence of metalloid-rich phases, Pd partitions preferentially into MSS (Cafagna and Jugo, 2016). Significant concentrations of Pd must partition into MSS at an early magmatic stage to account for high Pd concentrations in isolated pentlandite crystals (Osbahr et al., 2013). In the S-poor dunite zone of the Fazenda Mirabela intrusion, it is clear that Pt, Au, and semimetals have been lost through their partitioning into a fractionated Cu-rich sulfide liquid which was then largely removed by high temperature magmatic fluids and redistributed into the Santa Rita ore zone above. However, Pd was not removed during this process which suggests that it partitioned into MSS as it crystallized from the sulfide liquid, and not into the fractionated Cu-rich sulfide liquid. The partitioning of Pd directly into MSS and subsequently pentlandite as it recrystallizes, eliminates the need to invoke Pd diffusion from fractionated Cu-rich sulfides.

IPGE and cobalt in pyrite

Concentrations of IPGE and Co in pyrite are being increasingly recognized and are again identified in pyrite from the Santa Rita ore zone in the Fazenda Mirabela intrusion. Cobalt concentrations in particular are very high and much more enriched when compared to the Co concentrations measured in pentlandite, pyrrhotite, and chalcopyrite. The discovery of PGE in pyrite has been noted previously with Pd identified in pyrite in the Keivitsansarvi Ni-Cu-PGE deposit in northern Finland (Gervilla and Kojonen, 2002), and Ru and Pt identified in pyrite in the Main Sulfide Zone of the Great Dyke in Zimbabwe (Oberthür et al., 1997). However, the genesis of such concentrations was not discussed in detail until recently.

Secondary pyrite commonly replaces pyrrhotite and pentlandite during post-magmatic hydrothermal alteration and it may inherit the PGE concentrations of these magmatic sulfides (Dare et al. 2011; Piña et al. 2012; 2013; Smith 2014; Duran et al. 2015; Piña et al. 2016). In these cases, the PGE concentrations in pyrite match those of the pyrrhotite and pentlandite it has replaced.

Alternatively, magmatic pyrite may exsolve from S-rich MSS in small quantities at temperatures below ~700^{o}C (Naldrett et al., 1967). Pyrite that hosts higher concentrations of some PGE (typically the IPGE) than coexisting pyrrhotite and pentlandite is suggested to be magmatic, as it has not simply inherited the PGE content of the sulfides that secondary pyrite would have replaced (Lorand and Alard, 2011; Dare et al., 2011; Piña et al., 2012). However, these studies of PGE-bearing pyrite are in areas that have undergone extensive alteration, creating uncertainty in the process of pyrite formation; for example, the origin of PGE-

bearing idiomorphic pyrite in the Aguablanca Ni-Cu-PGE deposit is uncertain and may be either an exsolution product of MSS or the alteration product of pyrrhotite (Piña et al., 2012).

Furthermore, in the McCreedy East deposit at Sudbury, oscillatory zoning is observed in magmatic pyrite hosting higher IPGE concentrations than coexisting pyrrhotite and pentlandite, all of which are interpreted to have exsolved from MSS (Dare et al., 2011). However, this zoning is also considered a feature of secondary mineral replacement reactions, whereby pyrrhotite has been converted to pyrite (Duran et al., 2015). The enrichment of Co, Rh ± IPGE in pyrite could also be explained by a process of fluid-assisted solid-state diffusion from surrounding pentlandite and pyrrhotite, with semimetals, Pd, and Au introduced by the circulation of altering fluids (Piña et al., 2013; Duran et al., 2015).

Recent experimental work shows that pyrite exsolves from MSS during the cooling of a sulfide melt if the bulk S content is sufficiently high, and may incorporate significant amounts of Co, Ni, Ru, Rh, Os, Ir, and Pt, exhibiting a complex zonation of these elements similar to that observed in some natural occurrences (Cafagna and Jugo, 2016). This zoning is likely preserved due to slow diffusion rates in pyrite and can form during subsolidus reactions involving both MSS and ISS in the absence of hydrothermal processes (Cafagna and Jugo, 2016).

Several lines of evidence suggest that the pyrite in the Fazenda Mirabela intrusion is primary and has exsolved from MSS. Unlike other occurrences where PGE ± Co bearing pyrite has been identified, the Fazenda Mirabela intrusion is almost completely unaltered with no textural or chemical evidence for any significant alteration or secondary sulfide remobilization in the Santa Rita ore zone. This is also evidenced by euhedral pyrite occurring in the cores of interstitial sulfides intergrown with pentlandite (Fig. 4C, 10A, 10C, and 11F). Secondary pyrite would typically replace pyrrhotite at the edges of sulfide blebs which is not observed. Furthermore, pyrite hosts individual IPGE in greater concentrations than both pyrrhotite and pentlandite (excluding Ru in pentlandite which has an average of 0.9 ppm compared to 0.8 ppm in pyrite) suggesting that it has not simply replaced these sulfides and inherited their PGE content; this is also supported by the Pd-poor nature of pyrite. If pyrite had replaced pentlandite (commonly found intergrown with pyrite), one would expect pyrite to host Pd concentrations similar to that of pentlandite. The zoning of PGE in pyrite whereby these elements are enriched in the rim where in contact with other BMS and depleted in the core may suggest that the PGE have diffused from adjacent sulfides, with zoning preserved due to very slow diffusion rates of Os (and presumably the other PGE) in pyrite (Brenan et al., 2000; Cafagna and Jugo, 2016). However, such zoning is not observed in LA-ICP-MS data where laser traces cut rim-core sections of pyrite crystals (Fig. 17A), suggesting that the IPGE and Co have immediately partitioned into pyrite during its exsolution from MSS. This study, amongst others, suggests that primary magmatic pyrite should be considered as a potential host for the IPGE and Rh, as well as Co, particularly in a system with high PGE tenors (e.g., a PGE-reef type setting).

Conclusions

The understanding of PGE mineralization in the Fazenda Mirabela intrusion has been greatly improved by this study using a combination of geochemical and mineralogical

analyses with more than 700 platinum-group and precious metal minerals identified. The results from this work have wider implications for the behavior of PGE during the crystallization of immiscible sulfide melts.

During the crystallization of MSS in the S-poor dunite, Pt, Au, and the semimetals partitioned into a Cu-rich fractionated sulfide liquid which was subsequently largely removed and redistributed into the Santa Rita ore zone by high temperature magmatic fluids in a syn-magmatic process. This removal of semimetals significantly limited PGM formation in the S-poor dunite resulting in high PGE tenors in the remaining MSS which is poor in Pt, Au, and semimetals, but enriched in the IPGE, Rh, and Pd. This suggests that Pd does not partition into a Cu- or semimetal-rich fractionated melt as commonly suggested by experimental studies, and instead preferentially partitions into MSS. This explains the significant concentrations of Pd commonly identified in pentlandite without the need to invoke subsolidus diffusion from Cu-sulfides during cooling.

It is increasingly recognized that pyrite can host significant concentrations of PGE. However, the origin of such pyrite is not clear in the studies completed to date, in which the sulfide-bearing igneous rocks are invariably altered. This PGE-bearing pyrite may be of primary magmatic origin where it exsolves from MSS during cooling, or it can be secondary, replacing primary sulfides such as pyrrhotite and pentlandite.. Pyrite in the Fazenda Mirabela intrusion is of unambiguous primary magmatic origin and appears to have exsolved from MSS during cooling evidenced by the lack of pervasive alteration, and the preservation of primary magmatic textures and chemistry throughout the intrusion. Furthermore, the IPGE and Co have partitioned into pyrite during its exsolution and have not diffused into pyrite from adjacent BMS evidenced by the lack of zoning that would be observed due to very slow PGE diffusion rates in pyrite. This study demonstrates that the IPGE and Co will preferentially partition into pyrite over pentlandite and pyrrhotite during their exsolution from MSS and that pyrite should not necessarily be disregarded as a PGE-barren sulfide.

Finally, the distribution of As-bearing PGM, with sperrylite and irarsite restricted to the northern and southern margins of the intrusion, is consistent with As incorporation from the country rocks either via crustal assimilation or leaching during syn-magmatic hydrothermal processes associated with the heat of magma emplacement.

Acknowledgements

This study comprises part of Knight's PhD, completed at Cardiff University and supported by a Natural Environment Research Centre (NERC) research studentship (grant NE/I52787X/1). We would like to thank Mirabela Nickel Ltd. for additional support and assistance, and for allowing the publication of this data. We would like to thank two reviewers, Kevin Neyedley and Jacob Hanley, and editor Lawrence D. Meinert, for their constructive comments that have improved this paper.

References

Andersen, J.C.Ø., 2006, Postmagmatic sulphur loss in the Skaergaard Intrusion: Implications for the formation of the Platinova Reef: Lithos, v. 92, p. 198-221.

Ames, D.E., and Farrow, C.E.G., 2007, Metallogeny of the Sudbury mining camp, Ontario: Mineral Deposits Division, Geological Association of Canada Special Publication 5, p. 329−350.

Armitage, P.E.B., McDonald I., Edwards S.J., and Manby G.M., 2002, Platinum-group element mineralization in the Platreef and calc-silicate footwall at Sandsloot, Potgietersrus District, South Africa: Applied Earth Science (Transactions of the Institute of Mining and Metallurgy B), v. 111, p. 36-45.

Armitage, P.E.B., McDonald, I., and Tredoux, M., 2007, A geological investigation of the Waterberg hydrothermal platinum deposit, Mookgophong, Limpopo Province, South Africa: Applied Earth Science (Transactions of the Institute of Mining and Metallurgy B), v. 116, p. 113-129.

Ballhaus, C., and Sylvester, P., 2000, Noble Metal Enrichment Processes in the Merensky Reef, Bushveld Complex: Journal of Petrology, v. 41, p. 545-561.

Ballhaus, C., Tredoux, M., and Späth, A., 2001, Phase relations in the Fe-Ni-Cu-PGE-S system at magmatic temperature and application to massive sulphide ores of the Sudbury Igneous Complex: Journal of Petrology, v. 42, p. 1911-1926.

Barbosa, J.S.F., Gomes, L.C.C., Marinho, M.M., and Silva, F.C.A., 2003, Geologia do Segmento Sul do Orógeno Itabuna-Salvador-Curaçá: Revista Brasileira de Geociências, v. 33, p. 33-48.

Barbosa, J.S.F., and Sabaté, P., 2004, Archean and Paleoproterozoic crust of the São Francisco Craton, Bahia, Brazil: geodynamic features: *Precambrian Research*, v. 133, p. 1-27.

Barnes, S.J., Osborne, G.A., Cook, D., Barnes, L., Maier, W.D., and Godel, B., 2011, The Santa Rita Nickel Sulfide Deposit in the Fazenda Mirabela Intrusion, Bahia, Brazil: Geology, Sulfide Geochemistry, and Genesis: Economic Geology, v. 106, p. 1083-1110.

Barnes, S-J., Cox, R.A., and Zientek, M.L., 2006, Platinum-group element, Gold, Silver and Base Metal distribution in compositionally zoned sulfide droplets from the Medvezky Creek Mine, Noril'sk, Russia: Contributions to Mineralogy and Petrology, v. 152, p. 187-200.

Barnes, S-J., Prichard, H.M., Cox, R.A., Fisher, P.C., and Godel, B., 2008, The location of the chalcophile and siderophile elements in platinum-group element ore deposits (a textural, microbeam and whole rock geochemical study): Implications for the formation of the deposits: Chemical Geology, v. 248, p. 295-317.

Brenan, J.M., Cherniak, D.J., and Rose, L.A., 2000, Diffusion of osmium in pyrrhotite and pyrite: implications for closure of the Re–Os isotopic system: Earth and Planetary Science Letters, v. 180, p. 399-413.

Cafagna, F., and Jugo, P.J., 2016, An experimental study on the geochemical behavior of highly siderophile elements (HSE) and metalloids (As, Se, Sb, Te, Bi) in a mss-iss-pyrite system at 650° C: A possible magmatic origin for Co-HSE-bearing pyrite and the role of metalloid-rich phases in the fractionation of HSE: Geochimica et Cosmochimica Acta, v. 178, p. 233-258.

766 Dare, S.A.S., Barnes, S-J., Prichard, H.M., and Fisher, P.C., 2010a, The timing and formation
767 of platinum-group minerals from the Creighton Ni-Cu-Platinum-Group Element sulfide
768 deposit, Sudbury, Canada: Early crystallization of PGE-rich sulfarsenides: Economic
769 Geology, v. 105, p. 1071-1096.

770 Dare, S.A.S., Barnes, S-J., and Prichard, H.M., 2010b, The distribution of platinum group
771 elements (PGE) and other chalcophile elements among sulfides from the Creighton Ni–Cu–
772 PGE sulfide deposit, Sudbury, Canada, and the origin of palladium in pentlandite:
773 Mineralium Deposita, v. 45, p. 765-793.

774 Dare, S.A.S., Barnes, S-J., Prichard, H.M., and Fisher, P.C., 2011, Chalcophile and platinum-
775 group element (PGE) concentrations in the sulfide minerals from the McCreedy East deposit,
776 Sudbury, Canada, and the origin of PGE in pyrite: Mineralium Deposita, v. 46, p. 381-407.

777 Duran, C.J., Barnes, S-J., and Corkery, J.T., 2015, Chalcophile and platinum-group element
778 distribution in pyrites from the sulfide-rich pods of the Lac des Iles Pd deposits, Western
779 Ontario, Canada: Implications for post-cumulus re-equilibration of the ore and the use of
780 pyrite compositions in exploration: Journal of Geochemical Exploration, v. 158, p. 223-242.

781 Ferreira Filho, C.F., Cunha, E.M., Lima, A.C., Cunha, J.C., 2013. Depósito de Níquel-Cobre
782 Sulfetado de Santa Rita, Itagibá, Bahia, Brasil. Série Arquivos Abertos, v. 39, Companhia
783 Baiana de Pesquisa Mineral, p., 1-59.

784 Fleet, M.E., Chryssoulis, S.L., Stone, W.E., and Weisener, C.G., 1993, Partitioning of
785 platinum-group elements and Au in the Fe - Ni - Cu - S system: experiments on the fractional
786 crystallization of sulfide melt: Contributions to Mineralogy and Petrology, v. 115, p. 36-44.

787 Fuchs, W.A., and Rose, A.W., 1974, The geochemical behavior of platinum and palladium in
788 the weathering cycle in the Stillwater Complex, Montana: Economic Geology, v. 69, p. 332-
789 346.

790 Gervilla, F., and Kojonen, K., 2002, The platinum-group minerals in the upper section of the
791 Keivitsansarvi Ni-Cu-PGE deposit, Northern Finland: The Canadian Mineralogist, v. 40, p.
792 377-394.Godel B., and Barnes S-J., 2008a, Image analysis and composition of platinum-
793 group minerals in the J-M Reef, Stillwater Complex: Economic Geology, v. 103, p. 637-651.

794 Godel B., and Barnes S-J., 2008b, Platinum-group elements in sulphide minerals and the
795 whole rocks of the J-M Reef (Stillwater Complex): Implication for the formation of the reef:
796 Chemical Geology, v. 248, p. 272-294.

797 Godel, B., Barnes, S-J., and Maier, W.D., 2007, Platinum-Group Elements in Sulphide
798 Minerals, Platinum-Group Minerals, and Whole-Rocks of the Merensky Reef (Bushveld
799 Complex, South Africa): Implications for the Formation of the Reef: Journal of Petrology, v.
800 48, p. 1569-1604.

801 Hanley, J.J., 2005, The Aqueous Geochemistry of the Platinum Group Elements (PGE) in
802 Surficial, Low-T Hydrothermal and High-T Magmatic-Hydrothermal Environments, in
803 Mungall, J.E., ed., Exploration for platinum-group element deposits: Mineralogical
804 Association of Canada Short Course Series 35, Oulu, Finland, p. 35-56.

805 Hawley, J.E., 1965, Upside-down zoning at Frood, Sudbury, Ontario: Economic Geology, v.
806 60, p. 529-575.

807 Helmy, H.A., Ballhaus, C., Berndt, J., Bockrath, C., and Wohlgemuth-Ueberwassar, C., 2007,
808 Formation of Pt, Pd and Ni tellurides: experiments in sulfide-telluride systems: Contributions
809 to Mineralogy and Petrology, v. 153, p. 577-591.

810 Helmy, H.A., Ballhaus, C., Wohlgemuth-Ueberwassar, C., Fonseca, R.O.C., and Laurenz, V.,
811 2010, Partitioning of Se, As, Sb, Te and Bi between monosulfide solid solution and sulfide
812 melt - Application to magmatic sulfide deposits: Geochimica et Cosmochimica Acta, v. 74, p.
813 6174-6179.

814 Holwell, D.A., and McDonald, I., 2007, Distribution of platinum-group elements in the
815 Platreef at Overysel, northern Bushveld Complex: a combined PGM and LA-ICP-MS study:
816 Contributions to Mineralogy and Petrology, v. 154, p. 171-190.

817 Holwell D.A., and McDonald I., 2010. A review of the behaviour of platinum-group elements
818 within natural magmatic sulfide ore systems: The importance of semimetals in governing
819 partitioning behaviour: Platinum Metals Review, v. 54, p. 26-36.

820 Hutchinson D., and Kinnaird J.A., 2005, Complex multistage genesis for the Ni–Cu–PGE
821 mineralisation in the southern region of the Platreef, Bushveld Complex, South Africa:
822 Applied Earth Science (Transactions of the Institute of Mining and Metallurgy B), v. 114, p.
823 208-224.

824 Hutchinson, D., and McDonald, I., 2008, Laser ablation ICP-MS study of platinum-group
825 elements in sulfides from the Platreef at Turfspruit, northern limb of the Bushveld Complex,
826 South Africa: Mineralium Deposita, v. 43, p. 695-711.

827 Inwood, N., Smith, R., and Guzman, C., 2011, Santa Rita Project Technical Report, Mirabela
828 Nickel Ltd.

829 Keays, R.R., and Crocket, J.H., 1970, A Study of Precious Metals in the Sudbury Nickel
830 Irruptive Ores: Economic Geology, v. 65, p. 438-450.

831 Kinloch, E.D., 1982, Regional Trends in the Platinum-Group Mineralogy of the Critical Zone
832 of the Bushveld Complex, South Africa: Economic Geology, v. 77, p. 1328-1347.

833 Knight, R.D., Prichard, H.M., McDonald, I., and Ferreira Filho, C.F., 2011, Platinum-group
834 mineralogy of the Fazenda Mirabela intrusion, Brazil: the role of high temperature liquids
835 and sulphur loss: Applied Earth Science (Transactions of the Institute of Mining and
836 Metallurgy B), v. 120, p. 211-224.

837 Li, C., and Ripley, E.M., 2006, Formation of Pt-Fe alloy by desulfurization of Pt-Pd sulfide
838 in the J-M Reef of the Stillwater Complex, Montana: The Canadian Mineralogist, v. 44, p.
839 895-903.

840 Li, C., Barnes, S-J., Makovicky, E., Rose-Hansen, J., and Makovicky, M., 1996, Partitioning
841 of nickel, copper, iridium, rhenium, platinum, and palladium between monosulfide solid
842 solution and sulfide liquid: Effects of composition and temperature: Geochimica et
843 Cosmochimica Acta, v. 60, p. 1231-1238.

844 Li, C., Ripley, E.M., and Naldrett, A.J., 2003, Compositional variations of olivine and sulfur
845 isotopes in the Noril'sk and Talnakh intrusions, Siberia: Implications for ore-forming
846 processes in dynamic magma conduits: Economic Geology, v. 98, p. 69-86.

Lodders, K., 2003, Solar system abundances and condensation temperatures of the elements: Astrophysical Journal, v. 591, p. 1220–1247.

Lorand, J-P., and Alard, O., 2010, Pyrite tracks assimilation of crustal sulfur in Pyrenean peridotites: Contributions to Mineralogy and Petrology, v. 101, p. 151-128.

Mariga, J., Ripley, E.M., and Li, C., 2006, Petrologic evolution of gneissic xenoliths in the Voisey's Bay Intrusion, Labrador, Canada: Mineralogy, reactions, partial melting, and mechanisms of mass transfer: Geochemistry, Geophysics, Geosystems, v. 7, doi: 10.1029/2005GC001184.

McDonald, I., 2008, Platinum-group element and sulphide mineralogy in ultramafic complexes at western Andriamena, Madagascar: Applied Earth Science (Transactions of the Institute of Mining and Metallurgy B), v. 117, p. 1-10.

McDonald, I., Ohnenstetter, D., Rowe, J.P., Tredoux, M., Pattrick, R.A.D., and Vaughan, D.J., 1999, Platinum precipitation in the Waterberg deposit, Naboomspruit, South Africa: South African Journal of Geology, v. 102, p. 184-191.

Mungall, J.E., and Su, S., 2005, Interfacial tension between magmatic sulfide and silicate liquids: constraints on kinetics of sulfide liquation and sulfide migration through silicate rocks: Earth and Planetary Science Letters, v. 234, p. 135-149.

Mungall, J.E., Andrews, D.R.A., Cabri, L.J., Sylvester, P.J., and Tubrett, M., 2005, Partitioning of Cu, Ni, Au, and platinum-group elements between monosulfide solid solution and sulfide melt under controlled oxygen and sulfur fugacities: Geochimica et Cosmochimica Acta, v. 69, p. 4349-4360.

Naldrett, A.J., Craig, J.R., and Kullerud, G., 1967, The central portion of the Fe-Ni-S system and its bearing on pentlandite exsolution in iron-nickel sulfides ores: Economic Geology, v. 62, p. 826-847.

Naldrett, A.J., Innes, D.G., Sowa, J., and Gorton, M.P., 1982, Compositional variations within and between 5 Sudbury ore-deposits: Economic Geology, v. 77, p. 1519-1534.

Naldrett, A.J., Lightfoot, P.C., Fedorenko, V.A., Doherty, W., and Gorbachev, N.S., 1992, Geology and geochemistry of intrusions and flood basalts of the Norilsk region, USSR, with implications for the origin of the Ni-Cu ores: Economic Geology, v. 87, p. 975-1004.

Oberthür, T., Cabri, L.J., Weiser, T.W., McMahon, G., and Müller, P., 1997, Pt, Pd and other trace elements in sulfides of the Main Sulfide Zone, Great Dke, Zimbabwe: A reconnaissance study: The Canadian Mineralogist, v. 35, p. 597-609.

Osbahr, I., Klemd, R., Oberthür, T., Brätz, H., and Schouwstra, R., 2013, Platinum-group element distribution in base-metal sulfides of the Merensky Reef from the eastern and western Bushveld Complex, South Africa: Mineralium Deposita, v. 48, p. 211-232.

Peregoedova, A.V., 1998, The Experimental Study of the Pt-Pd-Partitioning between Monosulfide Solid Solution and Cu-Ni-Sulfide Melt at 900–840°C [ext. abs]: International Platinum Symposium, 8th, Johannesburg, South Africa, 1998, Extended Abstracts, p. 325-327.

886 Peregoedova, A.V., Barnes, S-J., and Baker, D.R., 2004, The formation of Pt-Ir alloys and
887 Cu-Pd-rich sulfide melts by partial desulfurization of Fe-Ni-Cu sulfides: results of
888 experiments and implications for natural systems: Chemical Geology, v. 208, p. 247-264.

889 Peucat, J.J., Barbosa, J.S.F, Araújo, I.C.P., Paquette, J.L., Martin, H., Fanning, M., Menezes,
890 A.B.L., Cruz, S., 2011, Geochronology of granulites from the south Itabuna-Salvador-Curaçá
891 Block, São Francisco Craton (Brazil): Nd isotopes and U-Pb zircon ages: Journal of South
892 American Earth Sciences, v. 31, p. 397-413.

893 Piña, R., Gervilla, F., Barnes, S-J., Ortega, L., and Lunar, R., 2012, Distribution of platinum-
894 group and chalcophile elements in the Aguablanca Ni-Cu sulfide deposit (SW Spain):
895 Evidence from a LA-ICP-MS study: Chemical Geology, v. 302–303, p. 61–75.

896 Piña, R., Gervilla, F., Barnes, S-J., Ortega, L., and Lunar, R., 2013, Partition Coefficients of
897 Platinum Group and Chalcophile Elements Between Arsenide and Sulfide Phases as
898 Determined in the Beni Bousera Cr-Ni Mineralization (North Morocco): Economic Geology,
899 v. 108, p. 935-951.

900 Piña, R., Gervilla, F., Barnes, S-J., Oberthür, T., and Lunar, R., 2016, Platinum-group
901 element concentrations in pyrite from the Main Sulfide Zone of the Great Dyke of
902 Zimbabwe: Mineralium Deposita, DOI 10.1007/s00126-016-0642-3.

903 Prichard, H.M., Ixer, R.A., Lord, R.A., Maynard, J., and Williams, N., 1994, Assemblages of
904 platinum-group minerals and sulphides in silicate lithologies and chromite-rich rocks within
905 the Shetland Ophiolite: The Canadian Mineralogist, v. 32, p. 271-294.

906 Prichard, H.M., Sá, J.H.S., and Fisher, P.C., 2001, Platinum-group mineral assemblages and
907 chromite composition in the altered and deformed Bacuri Complex, Amapa, Northeastern
908 Brazil: The Canadian Mineralogist, v. 39, p. 377-396.

909 Prichard, H.M., Knight, R.D., Fisher, P.C., McDonald, I., Zhou, M-F., and Wang, C.Y.,
910 2013, Distribution of platinum-group elements in magmatic and altered ores in the Jinchuan
911 intrusion, China: an example of selenium remobilization by postmagmatic fluids: Mineralium
912 Deposita, v. 48, p. 767-786.

913 Ripley, E.M., 1981, Sulfur Isotopic Studies of the Dunka Road Cu-Ni Deposit, Duluth
914 Complex, Minnesota: Economic Geology, v. 76, p. 610-620.

915 Ripley, E.M., and Alawi, J.A., 1986, Sulfide mineralogy and chemical evolution of the
916 Babbitt Cu-Ni deposit, Duluth Complex, Minnesota: The Canadian Mineralogist, v. 24, p.
917 347-368.

918 Ripley, E.M., and Aljassar, T.J., 1987, Sulfur and oxygen isotope studies of melt-country
919 rock interaction, Babbitt Cu-Ni deposit, Duluth Complex, Minnesota: Economic Geology, v.
920 82, p. 87-107.

921 Ripley E.M., and Li, C., 2013, Sulfide Saturation in Mafic Magmas: Is External Sulfur
922 Required for Magmatic Ni-Cu-(PGE) Ore Genesis?: Economic Geology, v. 108, p. 45-58.

923 Sá J.H.S., Barnes S.-J., Prichard H.P., and Fisher P.C., 2005, The Distribution of Base Metals
924 and Platinum-Group Elements in Magnetitite and Its Host Rocks in the Rio Jacaré Intrusion,
925 Northeastern Brazil: Economic Geology, v. 100, p. 333-348.

926 Samalens, N., Barnes, S.-J., and Sawyer, E.W., 2017, The role of black shales as a source of
927 sulfur and semimetals in magmatic nickel-copper deposits: Example from the Partridge River
928 Intrusion, Duluth Complex, Minnesota, USA: Ore Geology Reviews, v. 81, p. 173–187.

929 Seabrook, C.L., Prichard, H.M., and Fisher, P.C., 2004, Platinum-group minerals in the
930 Raglan Ni-Cu-(PGE) sulfide deposit, Cape Smith, Quebec, Canada: The Canadian
931 Mineralogist, v. 42, p. 485-497.

932 Smith, J.W., Holwell, D.A., and McDonald, I., 2014, Precious and base metal geochemistry
933 and mineralogy of the Grasvally Norite-Pyroxenite-Anorthosite (GNPA) member, northern
934 Bushveld Complex, South Africa: implications for a multistage emplacement: Mineralium
935 Deposita, v. 49, p. 667-692.

936 Suárez, S., Prichard, H.M., Velasco, F., Fisher, P.C., and McDonald, I., 2010, Alteration of
937 platinum-group minerals and dispersion of platinum-group elements during progressive
938 weathering of the Aguablanca Ni-Cu deposit, SW Spain: Mineralium Deposita, v. 45, p. 331-
939 350.

940 Wang, C.Y., Prichard, H.M., Zhou, M-F., and Fisher, P.C., 2008, Platinum-group minerals
941 from the Jinbaoshan Pd-Pt deposit, SW China: evidence for magmatic origin and
942 hydrothermal alteration: Mineralium Deposita, v. 43, p. 791-803.

943 Wood, S.A., 2002, The aqueous geochemistry of the platinum-group elements with
944 applications to ore deposits, in Cabri, L.J., ed., The Geology, Geochemistry, Mineralogy and
945 Mineral Beneficiation of the Platinum-group elements: Canadian Institute of Mining,
946 Metallurgy and Petroleum, Montreal, Special Volume 54, p. 211-249.

947 Wood S.A., and Normand C., 2008, Mobility of palladium chloride complexes in mafic
948 rocks: insights from a flow-through experiment at 25 ^{o}C using air-saturated, acidic, and Cl-
949 rich solutions: Mineralogy and Petrology, v. 92, p. 81-97.

950 Zientek, M.J., Cooper, R.W., Corson, S.R., and Geraghty, E.P., 2002, Platinum-group
951 elements mineralization in the Stillwater Complex, Montana, in Cabri, L.J., ed., The
952 Geology, Geochemistry, Mineralogy and Mineral Beneficiation of the Platinum-group
953 elements: Canadian Institute of Mining, Metallurgy and Petroleum, Montreal, Special
954 Volume 54, p. 459-481.

955

956

957

958

959

960

Table Captions:

Table 1: Depth, dip and azimuth information for all boreholes sampled from the central, northern and southern zones of the Fazenda Mirabela intrusion.

Table 2: Whole-rock semimetal and S concentrations for all samples studied from the southern zone boreholes MBS565 and MBS569. Abbreviations: Ol = olivine.

Table 3: Numbers of different platinum-group and precious metal minerals, sorted by type, identified from each zone of the intrusion (central, northern and southern) with the localized Pd-Cu alloy assemblage listed separately. Abbreviations: - = not detected

Table 4: Selective quantitative analyses and derived formulae of platinum-group and precious metal minerals from the northern and southern zones of the intrusion. Abbreviations: - = none observed

Table 5: Laser ablation-ICP-MS data for chalcopyrite, pentlandite, pyrrhotite, pyrite and BMS mixtures from the Santa Rita ore zone and basal PGE anomaly. Abbreviations: Cpy = chalcopyrite, Pn = pentlandite, Po = pyrrhotite, Py = pyrite, *n* = number of minerals analyzed, Ave = mean, Min = minimum value, Max = maximum value. * indicates isotopes where corrections have been applied for polyatomic or isobaric interferences.

Figure Captions:

Fig. 1. A. Map showing the location of the Fazenda Mirabela intrusion and simplified geology of the southern portion of the Itabuna-Salvador-Curaçá belt (modified after Barbosa et al., 2003; Barbosa and Sabaté, 2004). B. Map showing context and location of A within the major South American tectonic units. AC = Amazonian Craton; SF = São Francisco Craton.

Fig. 2. Geological map of the Fazenda Mirabela intrusion showing the location (projected to the surface) of the boreholes sampled; MBS209 and MBS158 from the northern zone, MBS604 and MBS605 from the central zone, and MBS565 and MBS569 from the southern zone (modified after Inwood et al., 2011). The W-E geological section, representative of the central zone of the intrusion, shows the location of borehole MBS604 (modified after Ferreira Filho et al., 2013).

Fig. 3. Geochemical profile of borehole MBS565 (southern zone) showing the position of the samples studied. The Santa Rita ore zone is defined by elevated S, Pt, and Pd concentrations (samples PTSR51-56). The basal PGE anomaly is present in dunite (samples PTSR58-60) and is characterized by elevated PGE, predominantly Pd, while remaining S-poor.

Fig. 4. Transmitted and reflected light photomicrographs, and back-scattered electron images showing the silicate and sulfide petrography of the Mirabela intrusion. A and B. Olivine and orthopyroxene with interstitial BMS demonstrating unaltered magmatic textures and minerals. C. Detailed image of BMS showing the relationship between pentlandite, euhedral pyrite, and chalcopyrite. D. Example of small finely disseminated sulfides in the S-poor dunite hosting the basal PGE anomaly. E and inset F. Example of micro-scale sulfide-silicate graphic textures resembling symplectites. BMS = base metal sulfides, Cpy = chalcopyrite, Cr = chromite, Opx = orthopyroxene, Ol = olivine, Pn = pentlandite, Py = pyrite, Sil = silicates.

1001 Fig. 5. Diagram showing the variation in chondrite normalized PGE profiles within the
1002 Fazenda Mirabela stratigraphy using samples from borehole MBS569. Pattern A. Negative
1003 Pd anomalies observed in the Santa Rita ore zone. Pattern B. Positive slopes without any
1004 significant anomalies in the transition between the Santa Rita ore zone and basal PGE
1005 anomaly. Pattern C. Positive Pd and negative Au (and Pt) anomalies in S-poor dunite samples
1006 from the basal PGE anomaly.

1007 Fig. 6. PGE ratio plots showing the variation in Pt, Pd, and Au concentrations between
1008 orthopyroxenite-harzburgite samples typically hosting the Santa Rita ore zone and S-poor
1009 dunite samples hosting the basal PGE anomaly. A. Variation in Pt/Pd ratios in dunite samples
1010 from the basal PGE anomaly and overlying orthopyroxenite samples. B. Variation in Au/Pd
1011 ratios in dunite samples from the basal PGE anomaly and overlying orthopyroxenite samples.

1012 Fig. 7. Plot demonstrating the significant correlation between Te (as a proxy for all
1013 semimetals) and S in whole-rock samples from boreholes MBS565 and MBS569 in the
1014 southern zone of the intrusion.

1015 Fig. 8. Schematic diagram showing the location of the different PGM assemblages identified;
1016 (i) predominately (Pt,Pd,Ni)(Fe,Bi,Te)$_2$ in the central zone, (ii) (Pt,Pd,Ni,Cu)(Fe,Bi,Te)$_2$ with
1017 As-bearing PGM at the margins of the intrusion, and (iii) the localized Pd-Cu alloy
1018 assemblage in the S-poor dunite in borehole MBS604 only.

1019 Fig. 9. Representative back-scattered electron images showing PGE tellurides from the
1020 northern and southern zones of the Fazenda Mirabela intrusion. A. Rounded Pd-Pt telluride
1021 within chalcopyrite. B. Rounded Ni-Pd telluride within pentlandite. C. Lath shaped Ni-Pt-Pd
1022 telluride within BMS, and crossing pyrite and chalcopyrite. D. Lath shaped Pt telluride at the
1023 edge of chalcopyrite and in contact with pyroxene. E. Pyrrhotite stringer hosting Pt-Ni-Fe
1024 telluride, both enclosed by a serpentine veinlet cutting olivine. F. Chalcopyrite stringer
1025 connecting to an interstitial sulfide bleb (pentlandite) hosting Ni-Pt-Pd telluride. Cpy =
1026 chalcopyrite, Ol = olivine, Pn = pentlandite, Po = pyrrhotite, Py = pyrite, Pyx = pyroxene,
1027 Serp = serpentine.

1028 Fig. 10. Representative back-scattered electron images showing As-bearing PGM from the
1029 northern and southern zones of the Fazenda Mirabela intrusion. A. Sperrylite within
1030 pentlandite. B. Sperrylite within and at the edge of pentlandite and in contact with pyroxene.
1031 C. Sperrylite associated with chalcopyrite, pyroxene and serpentine. D. Partial sperrylite
1032 stringer at the termination of an interstitial sulfide bleb. E. Sperrylite associated with BMS
1033 stringer (out of frame) cutting pyroxene. F. Platarsite-irarsite within pentlandite associated
1034 with pyrite. Cpy = chalcopyrite, Cr = chromite, Pn = pentlandite, Py = pyrite, Pyx =
1035 pyroxene, $PtAs_2$ = sperrylite, (Pt,Ir)AsS = platarsite-irarsite, Serp = serpentine.

1036 Fig. 11. Ternary diagram showing the variation in Ni, Pd, and Pt concentrations in PGE-
1037 tellurides. Atomic weight proportions plotted from semi-quantitative data derived from the
1038 SEM.

1039 Fig. 12. Representative back-scattered electron images showing accessory phases in the Santa
1040 Rita ore zone and PGM from the localized Pd-Cu alloy assemblage in the basal PGE anomaly
1041 in the central zone (MBS604 only). A. Hessite within and at the margins of pentlandite, and
1042 in contact with pyroxene. B. Hessite within and at the margins of pentlandite and pyrrhotite,
1043 and in contact with serpentine. C. Electrum with Cu and Fe within and at the edge of

chalcopyrite, and in contact with olivine and serpentine. D. Native Au within serpentine. E. and inset F. Pd-Cu alloys within pentlandite exhibiting micro-scale sulfide-silicate graphic textures that resemble symplectites. Ag_2Te = hessite, Cpy = chalcopyrite, Cr = chromite, Ol = olivine, Mgt = magnetite, Pn = pentlandite, Po = pyrrhotite, Pyx = pyroxene, Serp = serpentine.

Fig. 13. Histograms showing the percentage of different platinum-group and precious metal minerals types identified at different textural sites. A. All zones of the intrusion. B. The northern and southern zones of the intrusion only. The addition of central zone data does not significantly alter the histogram pattern demonstrating that the mineral associations are very similar, except in the case of the Pd-Cu alloy assemblage that is absent in the marginal zones.

Fig. 14. Pie charts showing the distribution of different platinum-group and precious metal minerals in the central zone versus the northern and southern zones of the intrusion. A and B. Proportion of the different PGM and PMM identified in the central zone (excluding the Pd-Cu alloy assemblage) calculated by the number and total area observed, respectively. C and D. Proportion of the different PGM and PMM identified in the northern and southern zones calculated by the number and total area observed, respectively. E and F. Proportion of the different PGM and PMM identified in the localized Pd-Cu alloy assemblage calculated by the number and total area observed, respectively.

Fig. 15. Histogram showing the difference in platinum-group and precious metal mineral size (in μm^2) from the Santa Rita ore zone and the basal PGE anomaly in the S-poor dunite.

Fig. 16. Stacked column plots showing the average concentrations of PGE in different sulfides determined by LA-ICP-MS. A. Sulfides analyzed from the Santa Rita ore zone. B. Sulfides analyzed from the basal PGE anomaly in the S-poor dunite.

Fig. 17. Plots of time resolved spectra from LA-ICP-MS traces through BMS from the Fazenda Mirabela intrusion. A. Pyrite-pentlandite from the Santa Rita ore zone with pyrite hosting significant Co, Os, and Ru. B. Pentlandite from the basal PGE anomaly in the S-poor dunite hosting high concentrations of Ir, Pd, and Pt.

Fig. 18. Schematic diagram demonstrating the formation of BMS stringers and their associated PGM. Temperatures are based on the crystallization temperatures of MSS and ISS, and exsolution temperatures of pentlandite, pyrrhotite, and chalcopyrite. A. Sulfide liquid coalesces as interstitial blebs to olivine and pyroxene. B. Compression from the growing silicate crystal pile forces the sulfide liquid into stringers along silicate grain boundaries in the direction of least resistance. C. The sulfide liquid crystallizes to form MSS and ISS. D. These phases re-crystallize to form pentlandite, pyrrhotite, pyrite, and chalcopyrite during subsolidus cooling. PGM exsolve from interstitial sulfides and BMS stringers during further cooling. Ol = olivine, Pn = pentlandite, Po = pyrrhotite, Py = pyrite, Pyx = pyroxene.

Fig. 19. Schematic diagram showing the formation of micro-scale sulfide-silicate graphic textures resembling symplectites and associated PGM from the basal PGE anomaly in the S-poor dunite. Temperatures are based on the crystallization temperatures of MSS and ISS, and exsolution temperatures of pentlandite, pyrrhotite, and chalcopyrite. A. Platinum, Au, and the semimetals partition into a fractionated Cu-rich sulfide liquid that forms during the crystallization of MSS. B. Small volumes of high temperature, volatile-rich, magmatic fluid with a high oxygen fugacity (f_{O_2}) removes a significant portion of this Cu-rich liquid

including the Pt, Au, and semimetals therein (and redistributes these elements into the overlying Santa Rita ore zone) replacing it with magnetite and phlogopite while the remainder crystallizes to form minor ISS. Further fluid/MSS interaction results in the formation of micro-scale sulfide-silicate graphic textures and FeS is partially-totally replaced by magnetite. C. Pentlandite and minor chalcopyrite recrystallizes from MSS and ISS, respectively, and small numbers of PGE-bearing minerals exsolve from the sulfides utilizing any remaining semimetals during subsolidus cooling; the majority of PGE are retained in solid solution in high tenor sulfides. D. In MBS604, high temperature fluids are channelized and almost all of the Cu-rich sulfide liquid is removed and replaced with phlogopite, minor bornite and magnetite. E. Further fluid/MSS interaction results in the formation of micro-scale sulfide-silicate graphic textures and FeS is partially-totally replaced by magnetite. F. Pentlandite recrystallizes from MSS and PGE exsolve from this sulfide phase primarily in the form of alloys in the absence of semimetals. Bn = bornite, Cpy = chalcopyrite, Mgt = magnetite, Ol = olivine, Phlog = phlogopite, Pn = pentlandite.

Tables:

Table 1

Borehole	Depth (m)	Dip	Azimuth
MBS604	1072	68°	270°
MBS605	1067	69°	270°
MBS209	356	60°	270°
MBS158	368	60°	270°
MBS565	630	61°	270°
MBS569	761	60°	270°

Table 2

Borehole	Sample No.	Lithology	As ppm	Bi ppm	Sb ppm	Te ppm	S wt. %
MBS565	PTSR0050	Websterite	0.20	< 0.02	< 0.02	< 0.02	0.15
MBS565	PTSR0051	Orthopyroxenite	0.80	0.05	< 0.02	0.72	0.47
MBS565	PTSR0052	Orthopyroxenite	0.70	0.07	0.03	0.89	0.70
MBS565	PTSR0053	Ol Orthopyroxenite	0.50	0.03	0.02	0.63	0.28
MBS565	PTSR0054	Harzburgite	0.20	< 0.02	0.08	0.26	0.14
MBS565	PTSR0055	Harzburgite	1.80	0.14	< 0.02	2.40	1.41
MBS565	PTSR0056	Harzburgite	1.50	0.15	0.03	2.46	1.40
MBS565	PTSR0057	Harzburgite	0.60	< 0.02	1.10	0.40	0.14
MBS565	PTSR0058	Dunite	0.20	< 0.02	0.03	0.19	0.05
MBS565	PTSR0059	Dunite	0.30	< 0.02	< 0.02	0.10	0.04
MBS565	PTSR0060	Dunite	0.20	< 0.02	0.02	0.08	0.04
MBS569	PTSR0061	Gabbronorite	0.20	< 0.02	0.04	0.02	0.08
MBS569	PTSR0062	Websterite	0.40	< 0.02	0.05	0.03	0.23
MBS569	PTSR0063	Orthopyroxenite	0.70	0.06	0.02	0.72	0.70
MBS569	PTSR0064	Ol Orthopyroxenite	1.50	0.21	0.06	2.77	1.84
MBS569	PTSR0065	Ol Orthopyroxenite	0.70	0.06	0.02	1.23	0.60
MBS569	PTSR0066	Ol Orthopyroxenite	4.10	0.13	0.08	1.52	0.84
MBS569	PTSR0067	Harzburgite	1.10	< 0.02	< 0.02	0.13	0.06
MBS569	PTSR0068	Harzburgite	1.00	< 0.02	< 0.02	0.30	0.15
MBS569	PTSR0069	Harzburgite	0.50	0.02	< 0.02	0.65	0.34
MBS569	PTSR0070	Dunite	< 0.1	< 0.02	< 0.02	0.12	0.06
MBS569	PTSR0071	Dunite	0.30	< 0.02	< 0.02	0.04	0.02
MBS569	PTSR0072	Dunite	0.10	< 0.02	< 0.02	0.02	0.02

Table 3

Zone	Platinum-group and precious metal mineral types							
	(Ni,Cu,Pt,Pd)$(Fe,Bi,Te)_2$	Ag-Pd-Te	Ag_2Te	$(Pt,Fe,Rh)As_2$	(Ir,Pt,Rh)AsS	Pd-(Cu,Pb)	Au-(Ag,Cu,Fe)	Total
Central	156	0	29	2	1	0	8	196
Northern	183	16	41	49	11	0	9	309
Southern	139	5	27	20	7	1	14	213
Localised PGE alloy	2	0	0	2	2	15	0	21
Total	480	21	97	73	21	16	31	739

Table 4

Borehole	Sample	Mineral No.	Quantitative analyses (wt. %)										Mineral composition
			Fe	Ni	Cu	As	Pd	Ag	Te	Pt	Bi	Total	
MBS158	PTSR-40	A1	-	18.97	-	-	0.41	-	80.52	-	-	99.90	$(Ni_{1.01}Pd_{0.01})_{1.02}Te_{1.98}$
MBS158	PTSR-40	H1	-	8.89	-	-	0.85	-	69.40	21.16	-	100.30	$(Ni_{0.56}Pt_{0.40}Pd_{0.03})_{0.99}Te_{2.01}$
MBS605	PTSR-22	B1	2.09	12.38	-	-	4.09	-	70.07	11.34	-	99.97	$(Ni_{0.71}Pt_{0.19}Pd_{0.13})_{1.03}(Te_{1.84}Fe_{0.13})_{1.97}$
MBS604	PTSR-07	F1	2.57	6.28		-	10.80	-	66.36	13.21	-	99.22	$(Ni_{0.38}Pd_{0.36}Pt_{0.24})_{0.98}(Te_{1.85}Fe_{0.17})_{2.02}$
MBS158	PTSR-46	H1	0.96	5.42			9.55		68.51	15.69	-	100.13	$(Ni_{0.34}Pd_{0.33}Pt_{0.30})_{0.97}(Te_{1.97}Fe_{0.06})_{2.03}$
MBS158	PTSR-40	K1	1.35	19.72	-	-	-	-	79.74	-	-	100.81	$Ni_{1.02}(Te_{1.90}Fe_{0.08})_{1.98}$
MBS158	PTSR-40	I1	1.64	18.65	-	-	-	-	76.99	-	2.71	99.99	$Ni_{0.99}(Te_{1.88}Fe_{0.09}Bi_{0.04})_{2.01}$
MBS158	PTSR-46	F1	-	4.41	-	-	6.13	-	65.68	24.25	-	100.47	$(Pt_{0.48}Ni_{0.29}Pd_{0.23})_{1.00}Te_{2.00}$
MBS158	PTSR-40	E1	-	-	-	-	-	62.02	37.91	-	-	99.93	$Ag_{1.98}Te_{1.02}$
MBS158	PTSR-40	M1	-	-	-	-	-	61.02	38.31	-	-	99.33	$Ag_{1.96}Te_{1.04}$
MBS565	PTSR-58	A1	-	-	-	42.60	-	-	-	57.12	-	99.72	$Pt_{1.02}As_{1.98}$
MBS569	PTSR-68	F1	-	-	-	44.27				56.67	-	100.94	$Pt_{0.99}As_{2.01}$
MBS569	PTSR-68	G1	-	-	34.62	-	-	-	65.93	-	-	100.55	$Cu_{1.03}Te_{0.97}$

Table 5

Mineral analyzed		Element	^{59}Co ppm	^{189}Os ppm	^{193}Ir ppm	^{99}Ru* ppm	^{103}Rh* ppm	^{195}Pt ppm	^{105}Pd ppm
Sulfides from the Santa Rita ore zone									
Cpy	*n=48*	Ave	201.22	0.03	<0.02	0.14	<0.10	0.05	0.27
		Min	0.09	<0.02	<0.02	<0.05	<0.10	<0.02	<0.20
		Max	1887.00	0.80	0.03	0.63	0.10	0.58	1.58
Pn	*n=95*	Ave	3026.20	0.52	0.09	0.91	0.11	0.03	2.31
		Min	670.00	<0.02	<0.02	<0.05	<0.10	<0.02	<0.20
		Max	7313.00	4.49	0.91	6.36	1.13	0.73	12.97
Po	*n=36*	Ave	65.57	0.55	0.11	0.58	0.04	0.07	0.01
		Min	1.29	0.00	<0.02	<0.05	<0.10	<0.02	<0.20
		Max	615.20	3.80	0.90	5.73	1.03	1.58	0.52
Py	*n=38*	Ave	16671.29	0.61	0.18	0.78	0.14	0.03	0.12
		Min	8569.00	<0.02	<0.02	<0.05	<0.10	<0.02	<0.20
		Max	32030.00	2.16	1.00	3.68	0.77	0.14	1.52
Sulfides from the basal PGE anomaly in the S-poor dunite									
Cpy	*n=3*	Ave	515.71	<0.02	0.07	0.06	<0.10	0.08	8.81
		Min	18.84	0.00	<0.02	<0.05	<0.10	<0.02	0.52
		Max	1346.00	0.00	0.12	0.12	<0.10	0.24	15.90
Pn	*n=27*	Ave	5913.33	4.22	1.74	6.28	4.33	4.33	42.47
		Min	2416.00	<0.02	<0.02	<0.05	<0.10	<0.02	3.88
		Max	9761.00	38.25	28.69	59.13	36.15	28.89	254.30
Pn-Cpy mix	*n=8*	Ave	5561.50	1.16	0.57	3.33	2.21	2.57	42.42
		Min	1367.00	<0.02	<0.02	<0.05	<0.10	<0.02	0.80
		Max	8910.00	5.18	2.61	11.48	8.82	14.70	124.89
Py	*n=2*	Ave	10915.00	3.52	1.57	2.80	<0.10	<0.02	0.37
		Min	9920.00	0.96	0.67	<0.05	<0.10	<0.02	0.26
		Max	11910.00	6.08	2.48	5.61	<0.10	<0.02	0.49
Pn-Py mix	*n=1*	n/a	5750.00	0.30	27.87	1.37	0.68	12.50	570.40
Pn-Py-Cpy mix	*n=1*	n/a	3245.00	0.04	18.68	1.63	<0.10	6.20	371.70

1166 Fig. 1

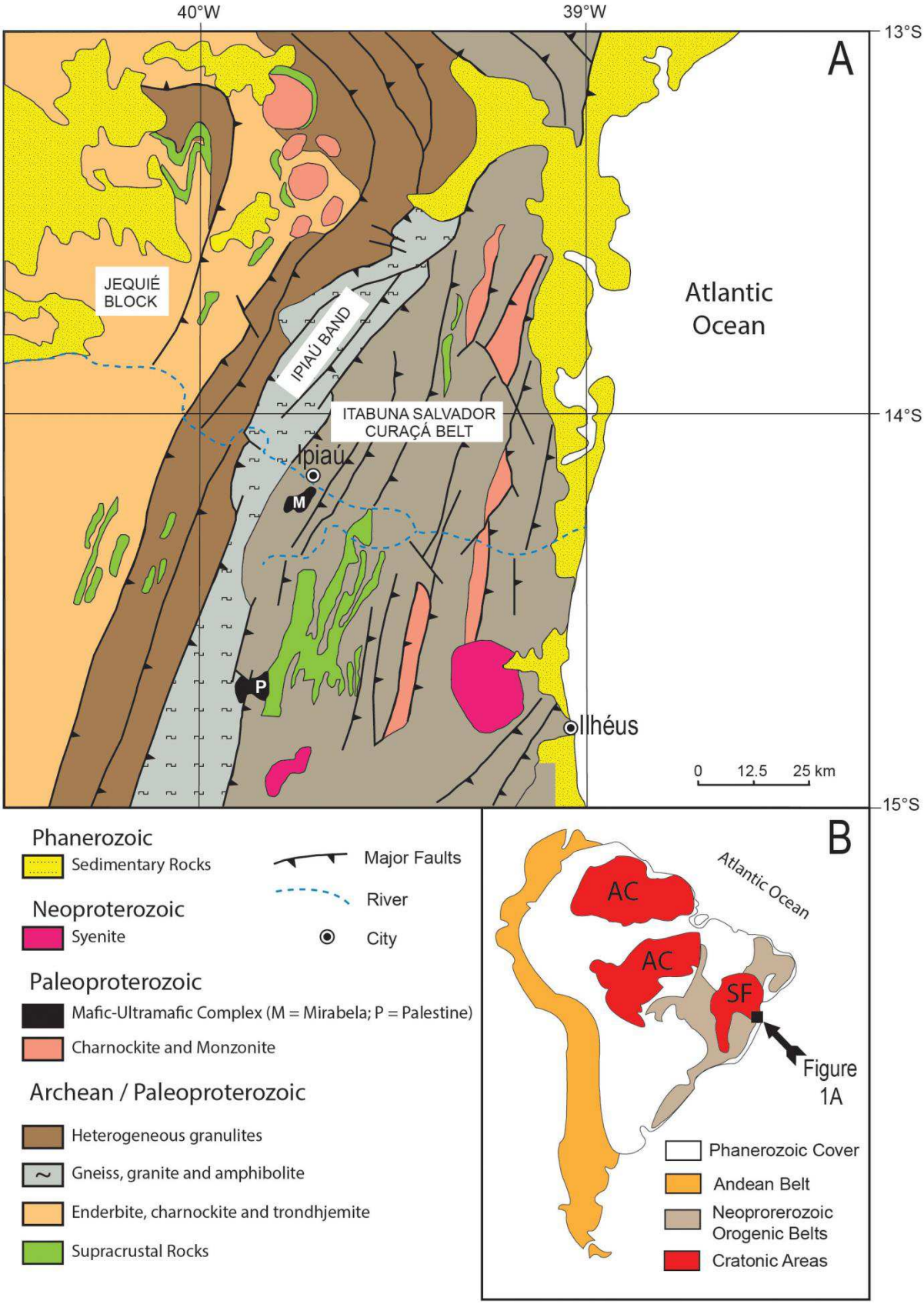

1167

1168

1169 Fig. 2

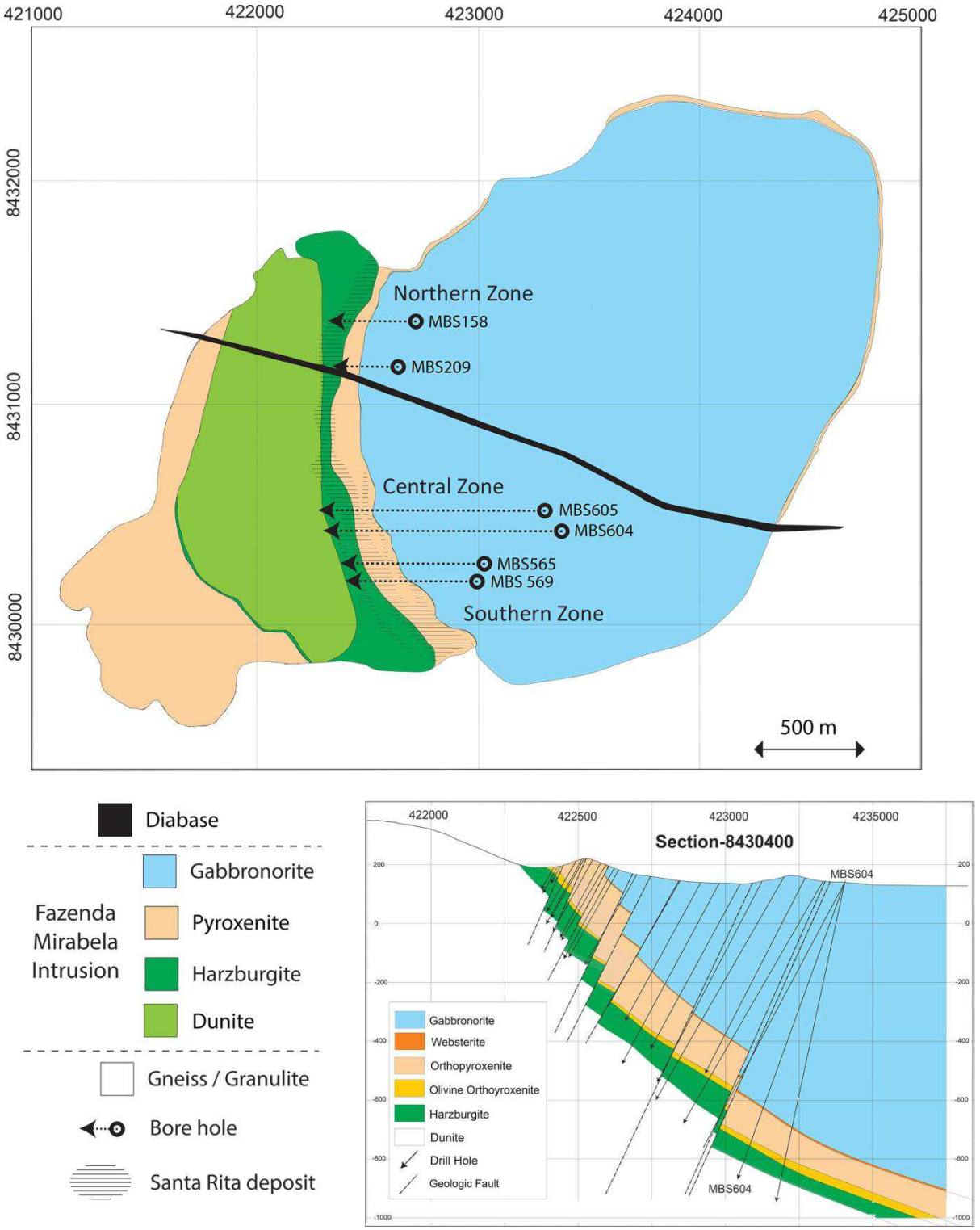

1170

1171

1172

1173

1174

Fig. 3

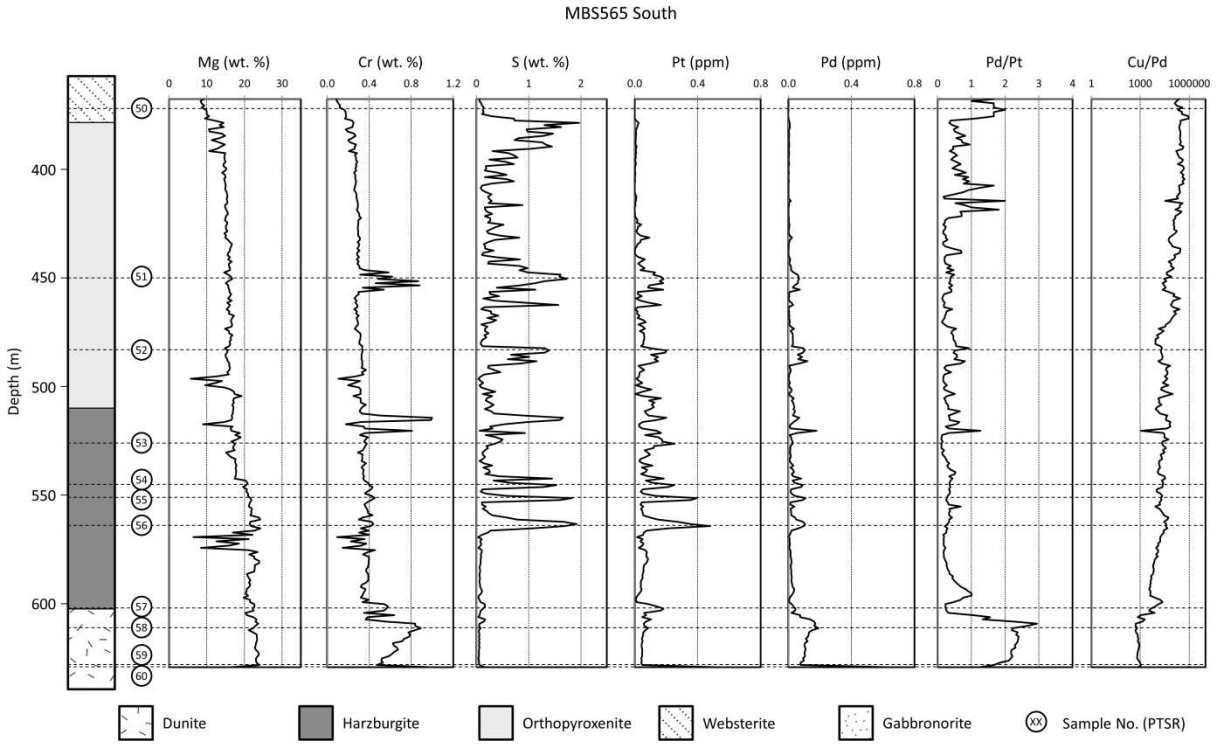
MBS565 South
Mg (wt. %)
Cr (wt. %)
S (wt. %)
Pt (ppm)
Pd (ppm)
Pd/Pt
Cu/Pd
Depth (m)
400
450
500
550
600
50
51
52
53
54
55
56
57
58
59
60
Dunite
Harzburgite
Orthopyroxenite
Websterite
Gabbronorite
XX Sample No. (PTSR)

Fig. 4

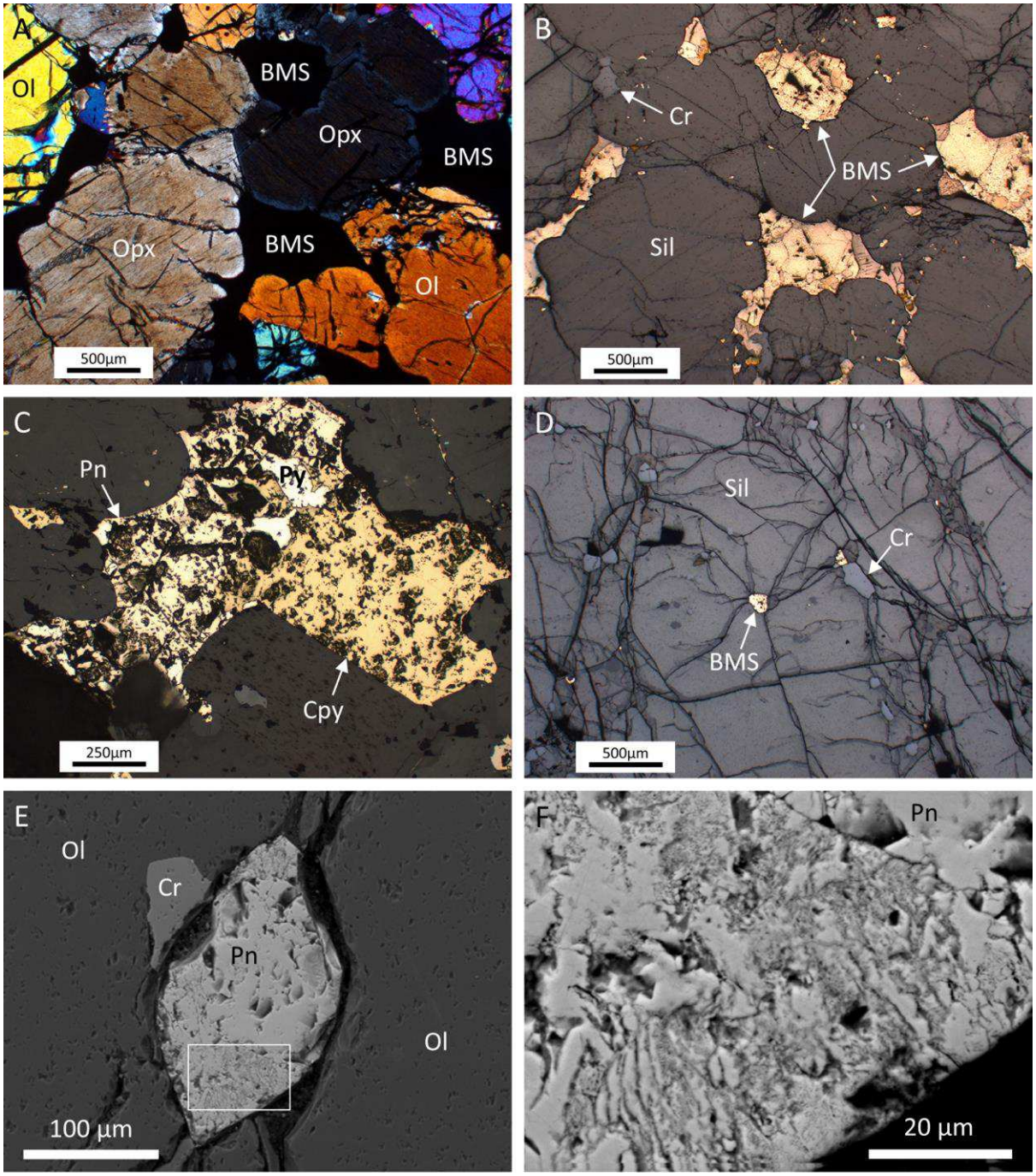
A
Ol
BMS
Opx
BMS
Opx
BMS
Ol
500µm
B
Cr
BMS
Sil
500µm
C
Pn
Py
Cpy
250µm
D
Sil
Cr
BMS
500µm
E
Ol
Cr
Pn
Ol
100 µm
F
Pn
20 µm

1203 Fig. 5

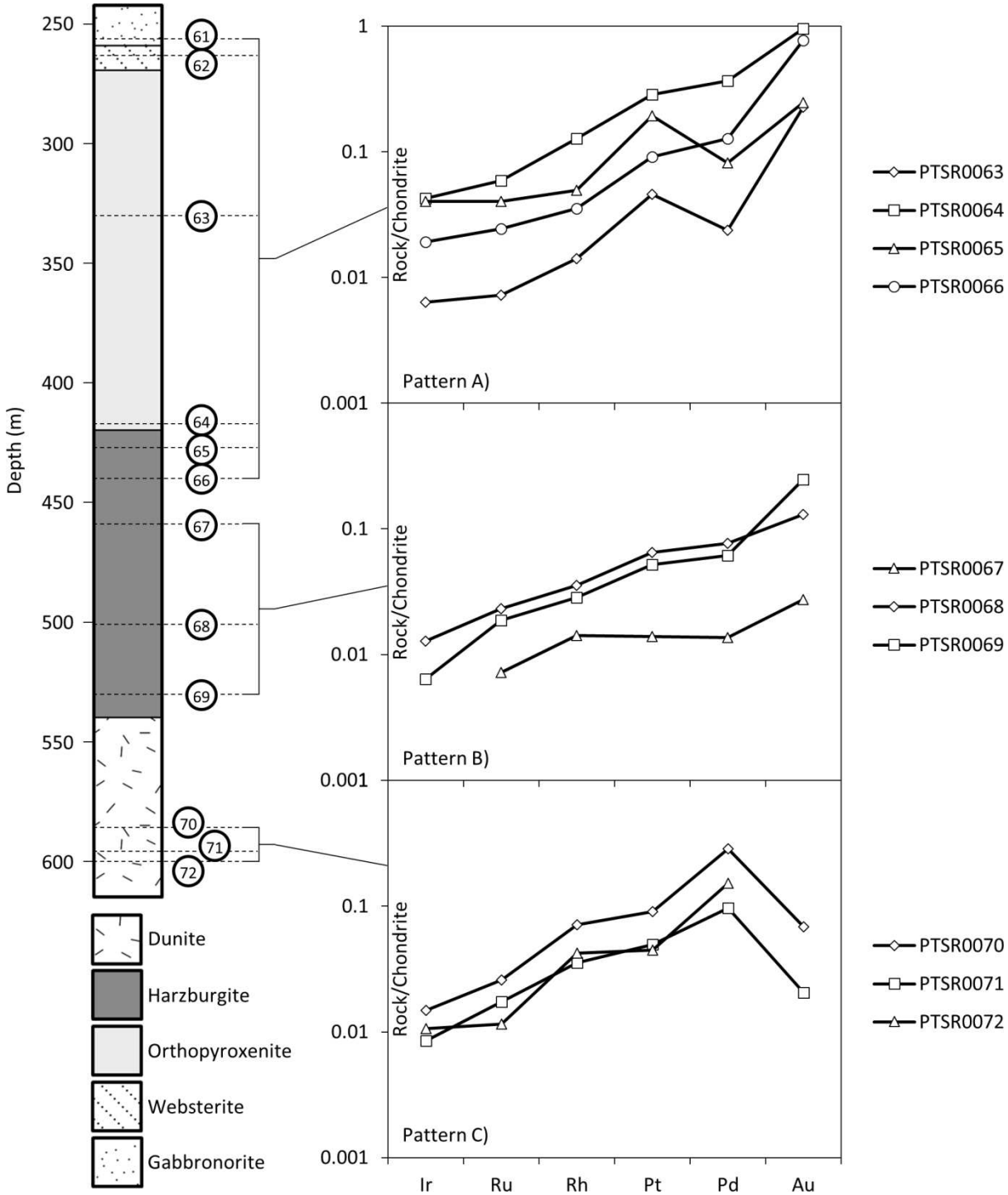

1204

1205

1206

1207

1208

1209

Fig. 6

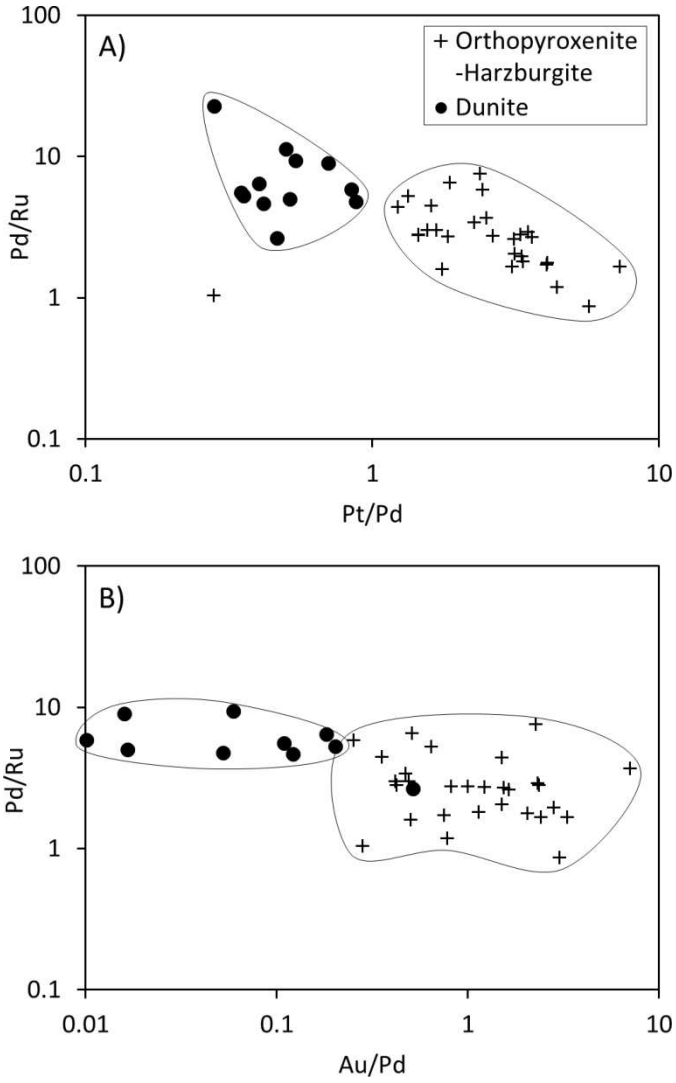
A)
+ Orthopyroxenite
-Harzburgite
● Dunite
Pd/Ru
Pt/Pd
100
10
1
0.1
0.1
1
10
B)
Pd/Ru
Au/Pd
100
10
1
0.1
0.01
0.1
1
10

Fig. 7

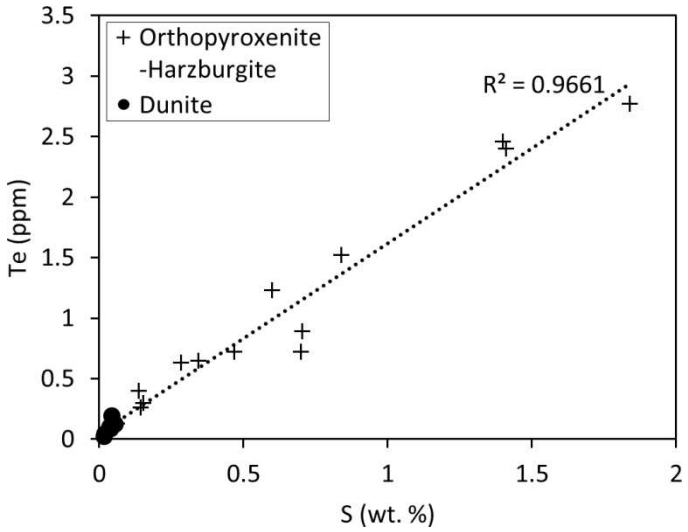
+ Orthopyroxenite
-Harzburgite
● Dunite
R² = 0.9661
Te (ppm)
S (wt. %)
0
0.5
1
1.5
2
2.5
3
3.5

Fig. 8

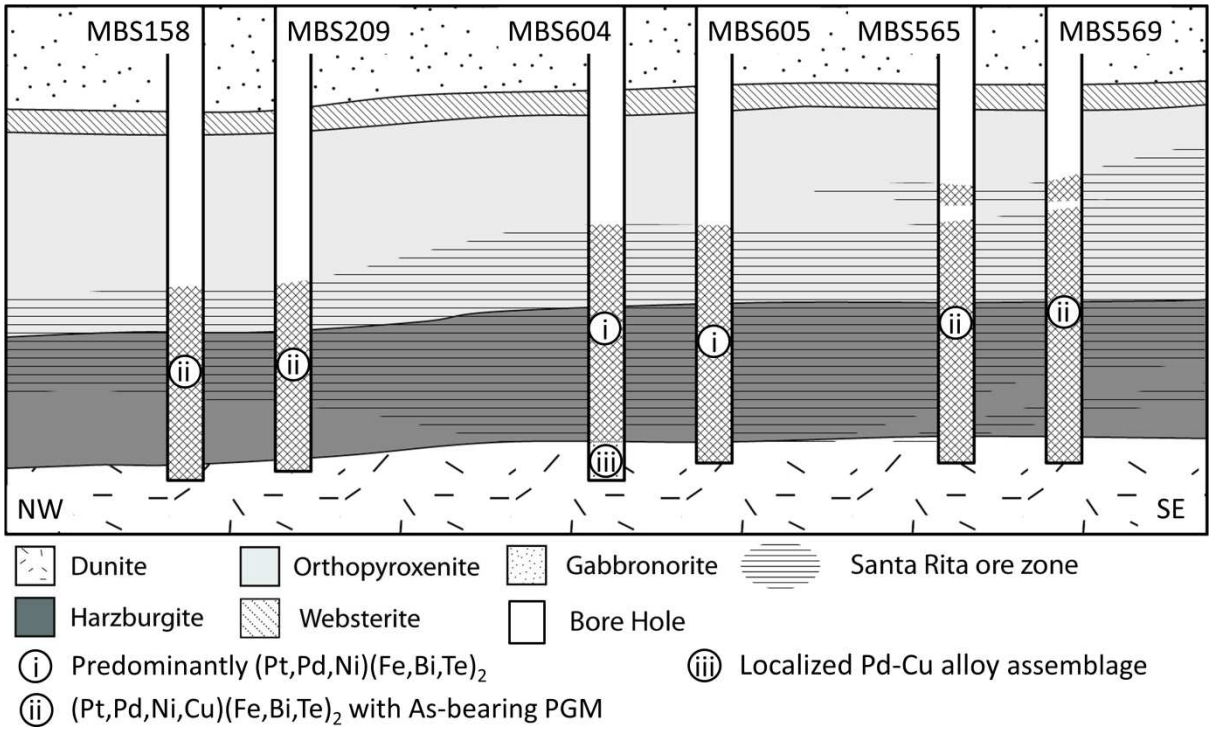
MBS158
MBS209
MBS604
MBS605
MBS565
MBS569
NW
SE
Dunite
Orthopyroxenite
Gabbronorite
Santa Rita ore zone
Harzburgite
Websterite
Bore Hole
(i) Predominantly (Pt,Pd,Ni)(Fe,Bi,Te)2
(iii) Localized Pd-Cu alloy assemblage
(ii) (Pt,Pd,Ni,Cu)(Fe,Bi,Te)2 with As-bearing PGM

1264 Fig. 9

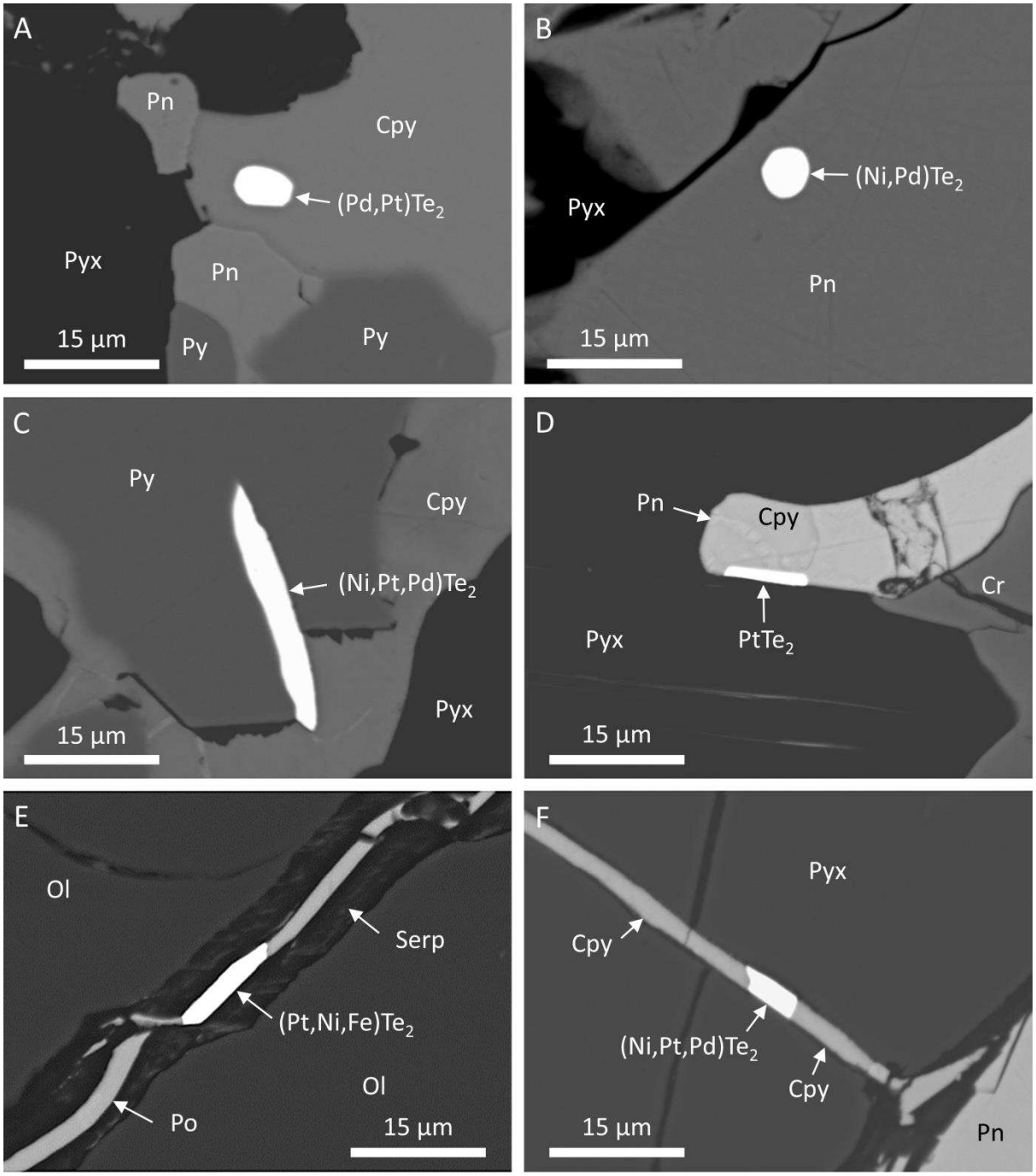

1265
1266
1267
1268
1269
1270
1271
1272

Fig. 10

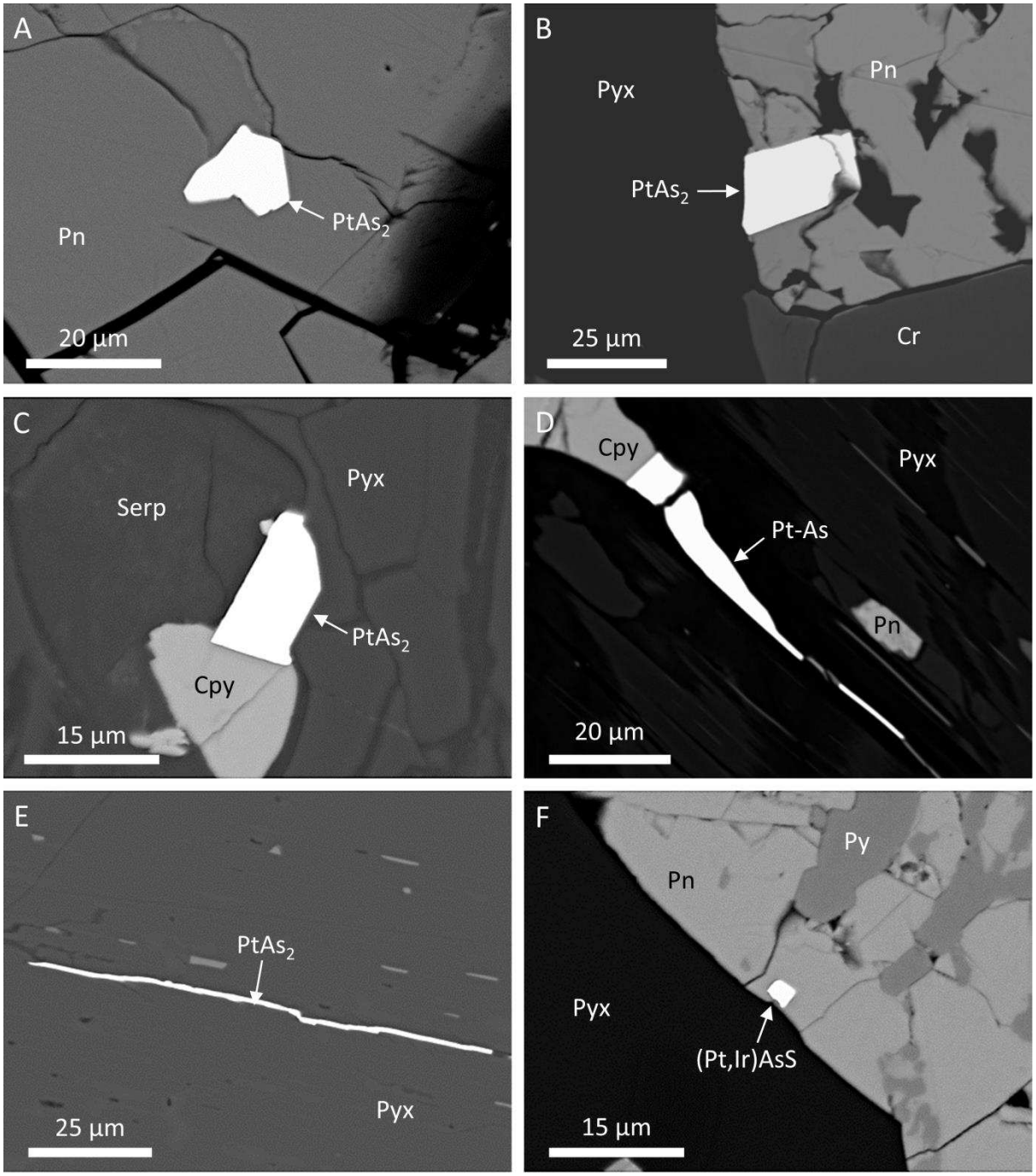
A
Pn
PtAs2
20 µm
B
Pyx
Pn
PtAs2
25 µm
Cr
C
Serp
Pyx
PtAs2
Cpy
15 µm
D
Cpy
Pyx
Pt-As
Pn
20 µm
E
PtAs2
25 µm
Pyx
F
Py
Pn
Pyx
(Pt,Ir)AsS
15 µm

Fig. 11

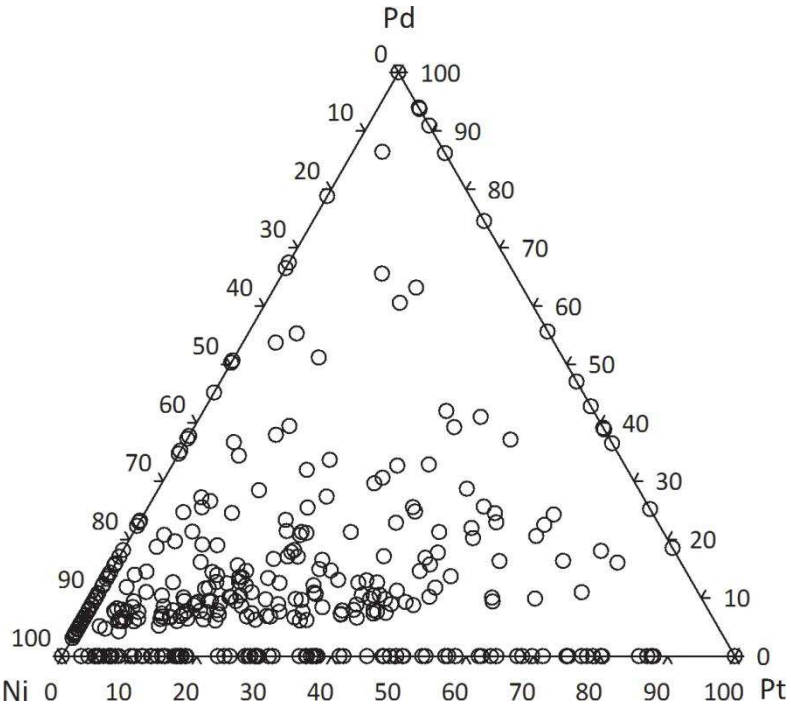
Pd
0
100
10
90
20
80
30
70
40
60
50
50
60
40
70
30
80
20
90
10
100
0
Ni 0 10 20 30 40 50 60 70 80 90 100 Pt

Fig. 12

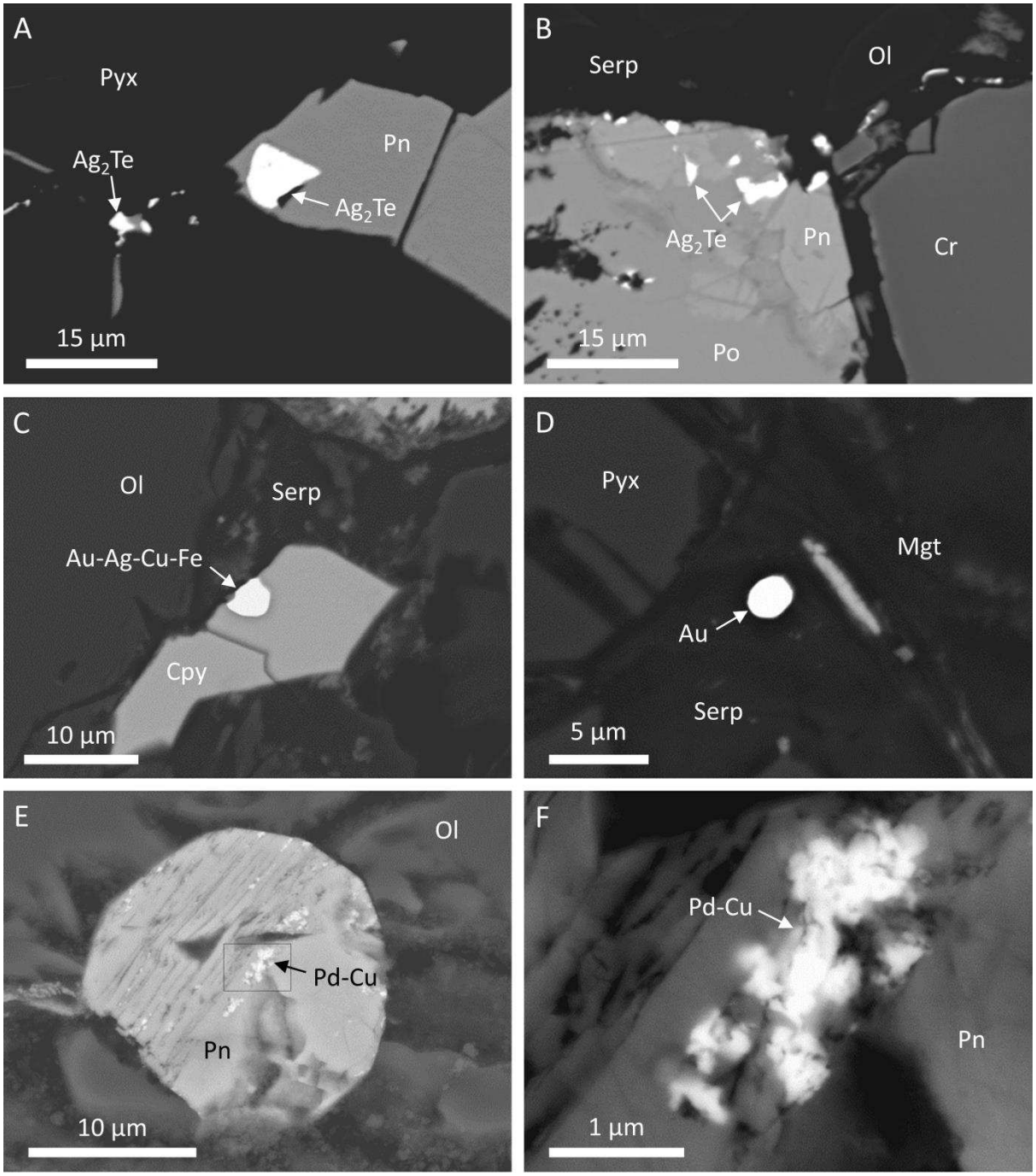
A
Pyx
Pn
Ag_2Te
Ag_2Te
15 µm
B
Serp
Ol
Ag_2Te
Pn
Cr
15 µm
Po
C
Ol
Serp
Au-Ag-Cu-Fe
Cpy
10 µm
D
Pyx
Mgt
Au
Serp
5 µm
E
Ol
Pd-Cu
Pn
10 µm
F
Pd-Cu
Pn
1 µm

Fig. 13

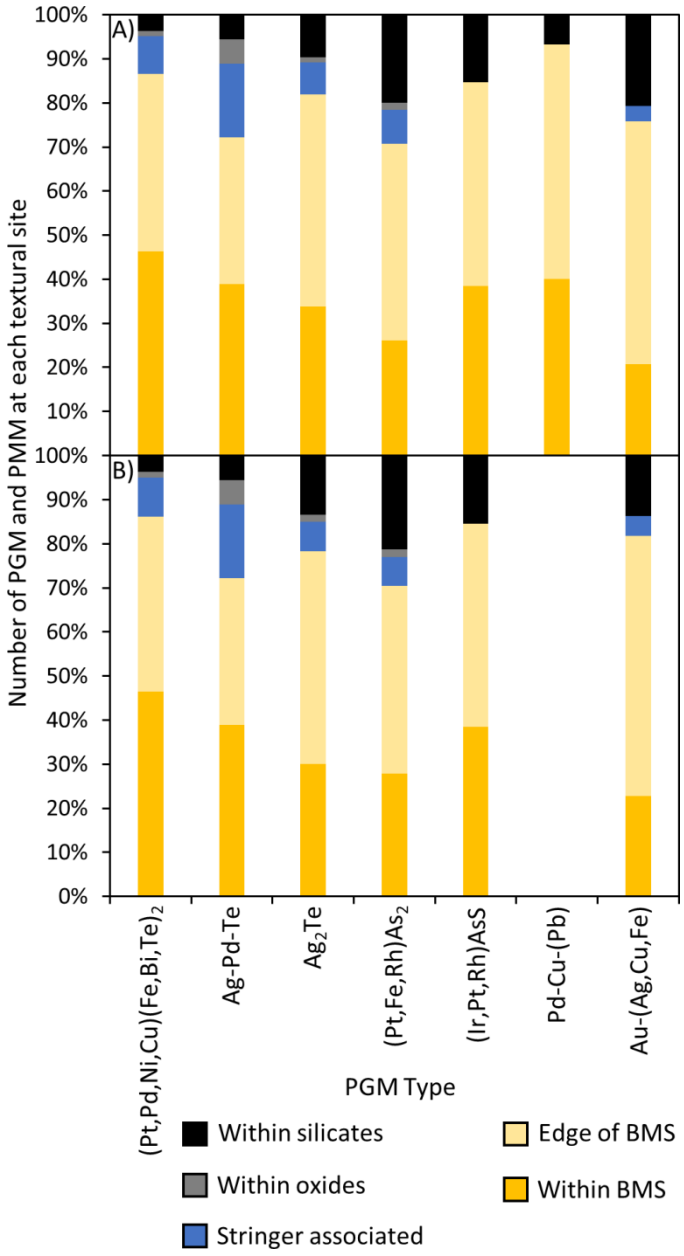
A)
B)
100%
90%
80%
70%
60%
50%
40%
30%
20%
10%
0%
Number of PGM and PMM at each textural site
(Pt,Pd,Ni,Cu)(Fe,Bi,Te)2
Ag-Pd-Te
Ag2Te
(Pt,Fe,Rh)As2
(Ir,Pt,Rh)AsS
Pd-Cu-(Pb)
Au-(Ag,Cu,Fe)
PGM Type
Within silicates
Within oxides
Stringer associated
Edge of BMS
Within BMS

Fig. 14

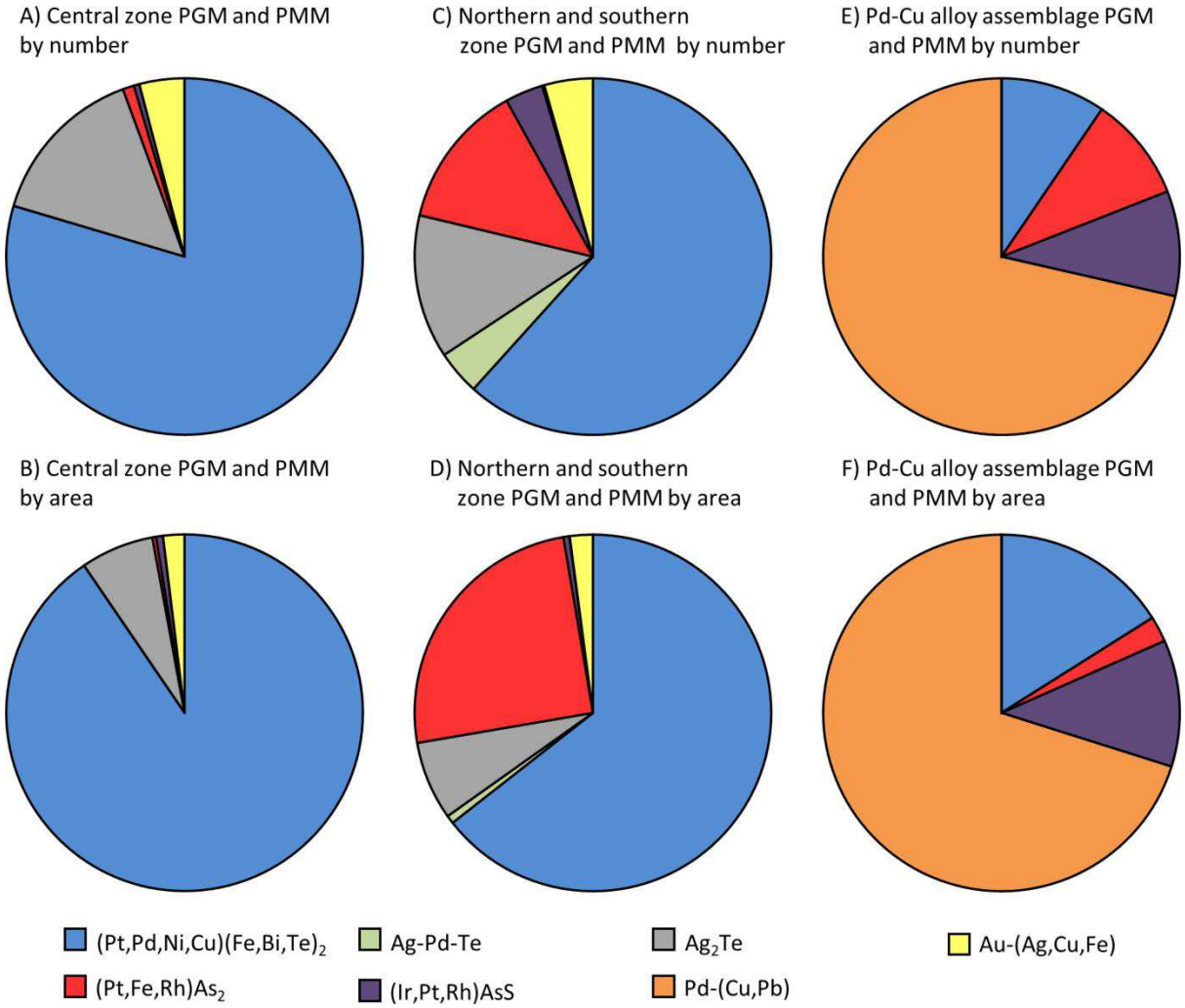
A) Central zone PGM and PMM by number
C) Northern and southern zone PGM and PMM by number
E) Pd-Cu alloy assemblage PGM and PMM by number
B) Central zone PGM and PMM by area
D) Northern and southern zone PGM and PMM by area
F) Pd-Cu alloy assemblage PGM and PMM by area
(Pt,Pd,Ni,Cu)(Fe,Bi,Te)2
Ag-Pd-Te
Ag2Te
Au-(Ag,Cu,Fe)
(Pt,Fe,Rh)As2
(Ir,Pt,Rh)AsS
Pd-(Cu,Pb)

Fig. 15

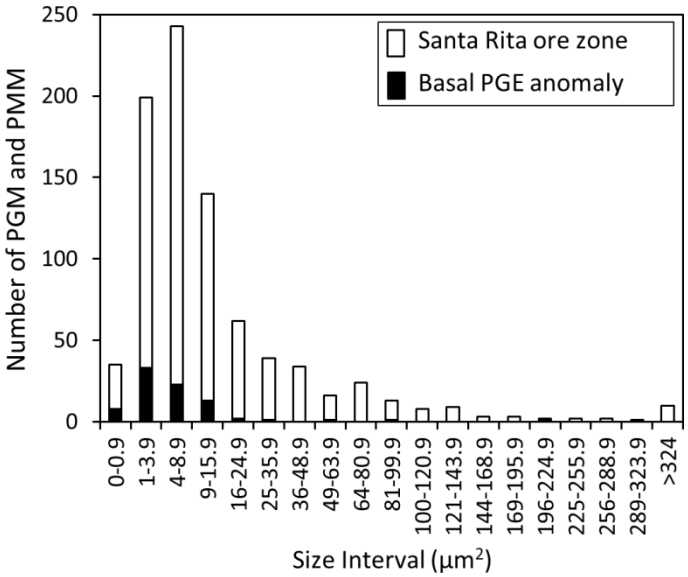
Santa Rita ore zone
Basal PGE anomaly
Number of PGM and PMM
250
200
150
100
50
0
0-0.9
1-3.9
4-8.9
9-15.9
16-24.9
25-35.9
36-48.9
49-63.9
64-80.9
81-99.9
100-120.9
121-143.9
144-168.9
169-195.9
196-224.9
225-255.9
256-288.9
289-323.9
>324
Size Interval (µm²)

Fig. 16

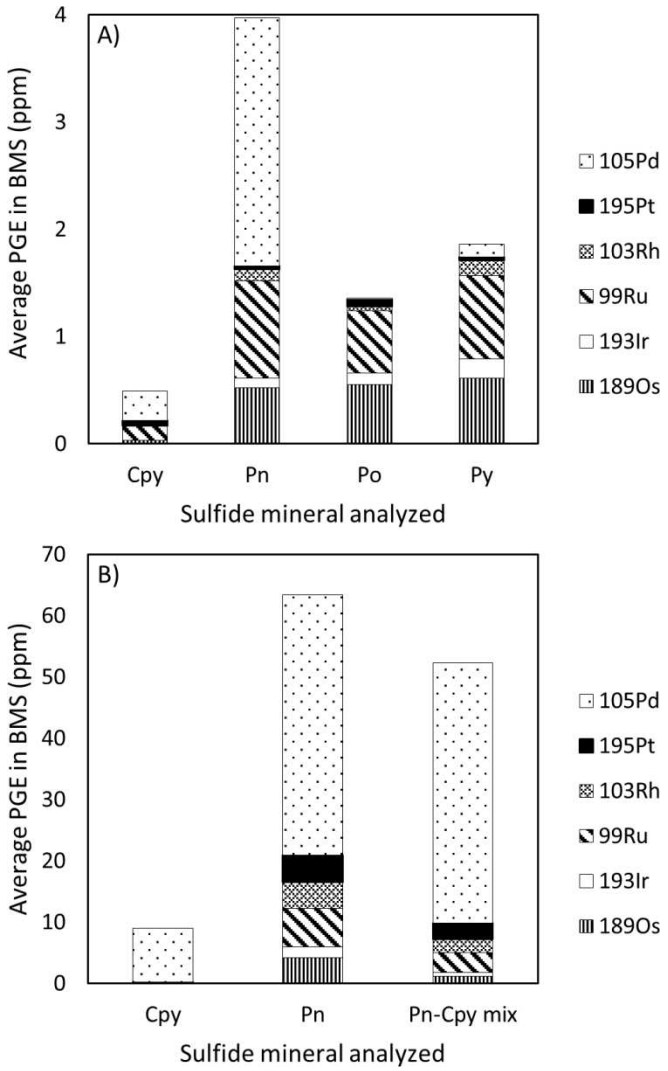
A)
Average PGE in BMS (ppm)
0
1
2
3
4
Cpy
Pn
Po
Py
Sulfide mineral analyzed
105Pd
195Pt
103Rh
99Ru
193Ir
189Os
B)
Average PGE in BMS (ppm)
0
10
20
30
40
50
60
70
Cpy
Pn
Pn-Cpy mix
Sulfide mineral analyzed
105Pd
195Pt
103Rh
99Ru
193Ir
189Os

Fig. 17

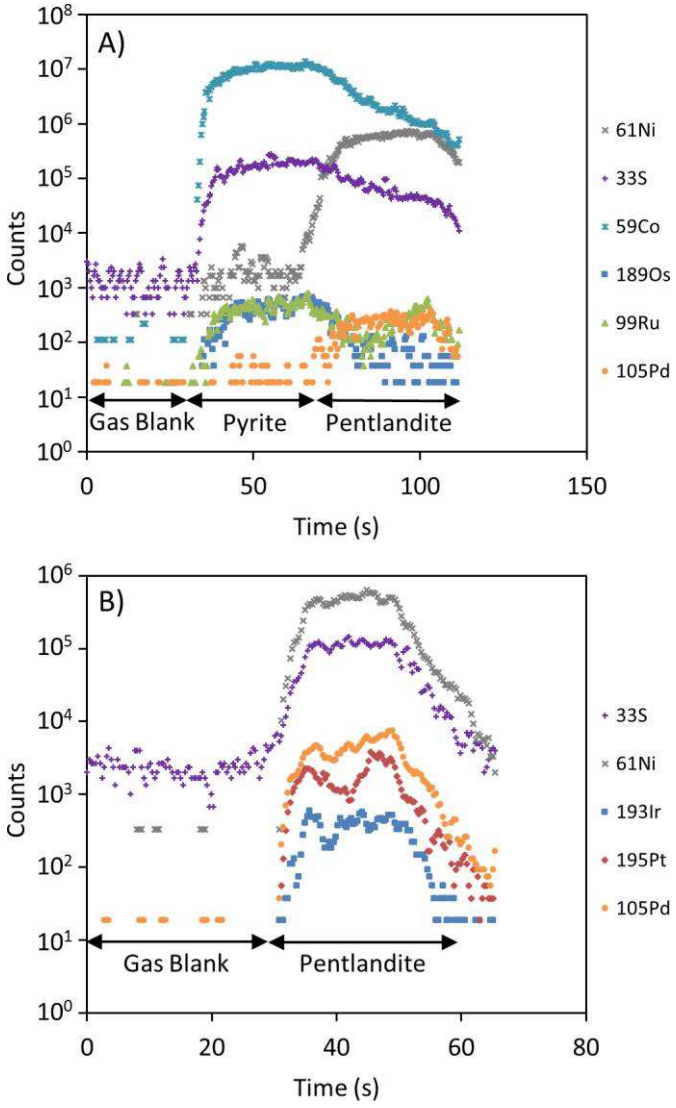
A)
Counts
Time (s)
61Ni
33S
59Co
189Os
99Ru
105Pd
Gas Blank
Pyrite
Pentlandite
B)
Counts
Time (s)
33S
61Ni
193Ir
195Pt
105Pd
Gas Blank
Pentlandite

Fig. 18

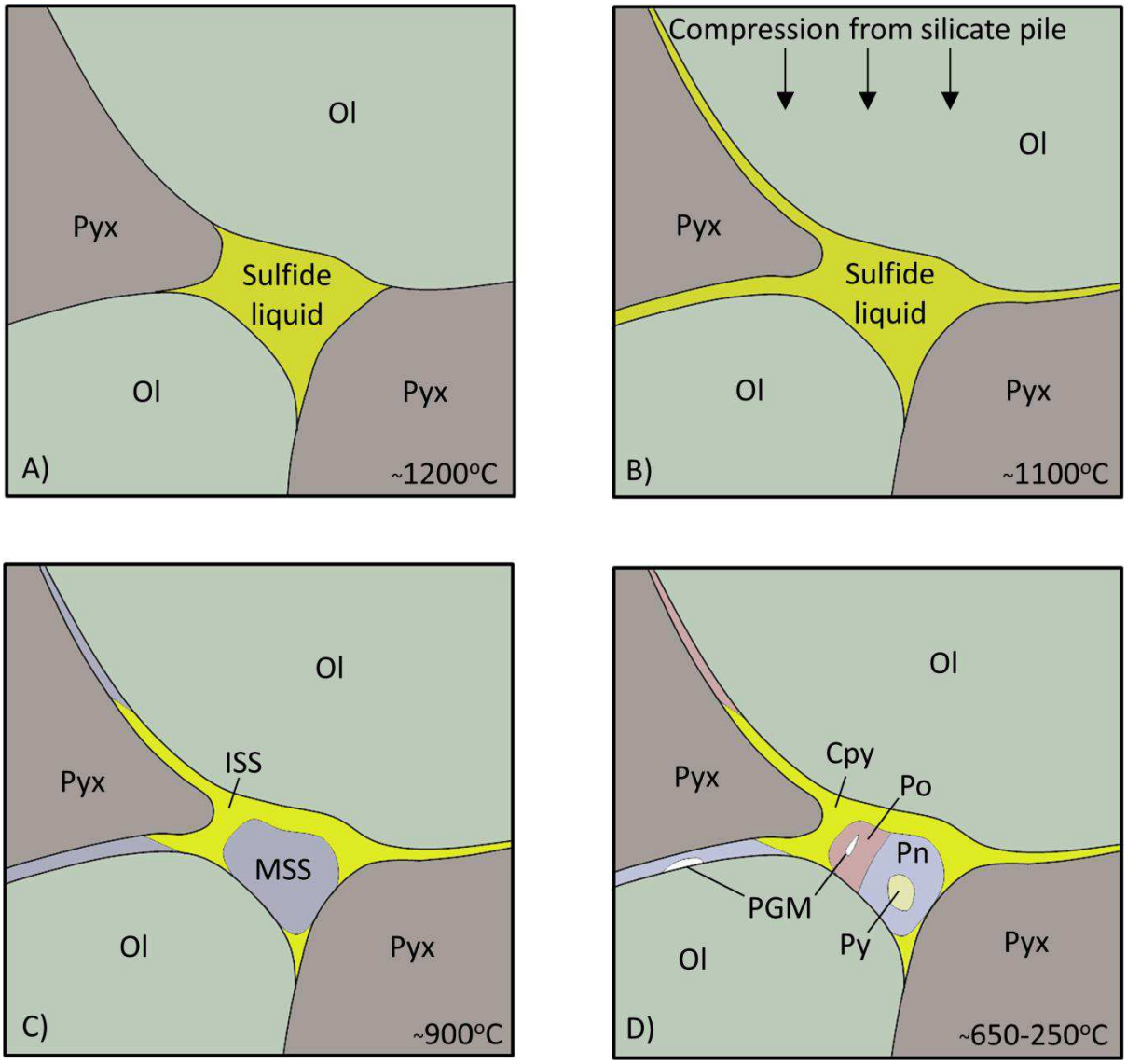
Ol
Pyx
Sulfide liquid
Ol
Pyx
A)
~1200°C
Compression from silicate pile
Ol
Pyx
Sulfide liquid
Ol
Pyx
B)
~1100°C
Ol
Pyx
ISS
MSS
Ol
Pyx
C)
~900°C
Ol
Pyx
Cpy
Po
Pn
PGM
Py
Ol
Pyx
D)
~650-250°C

1397 Fig. 19

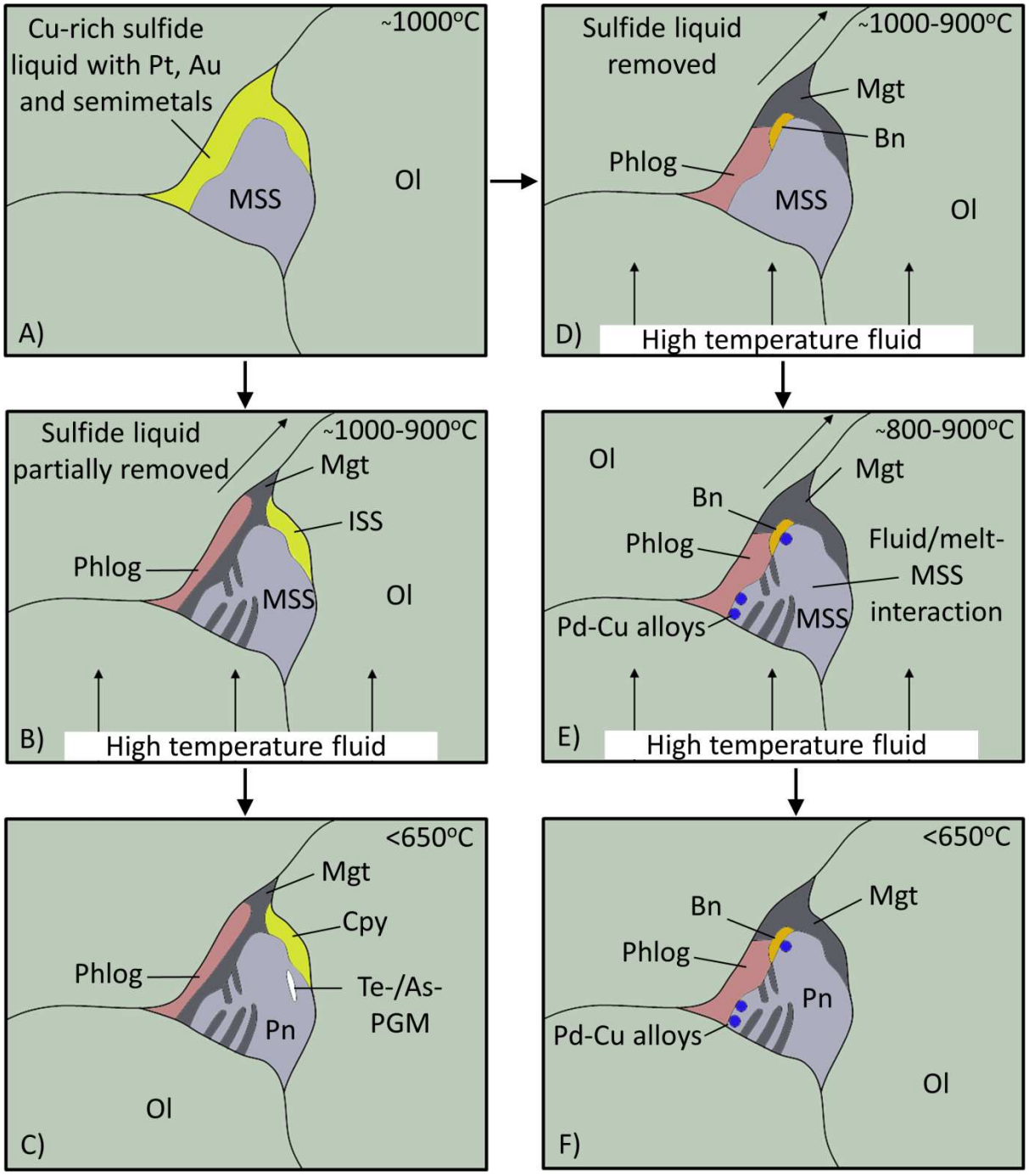

1398